University of Bayreuth

Micrometeorology Group

Bachelor Thesis

B.Sc. Geoecology, Micrometeorology

Quantifying the summer urban canopy layer heat island in a mid-sized central European city from noon to midnight:

Effects of land use on spatial patterns and turbulent energy fluxes

Lars Spakowski

September 2025

supervised by

Prof. Dr. Christoph Thomas

Abstract

Increased summertime mortality rates are associated with high temperatures in central European cities, showing the urgency for a fundamental understanding of the processes that shape the urban boundary layer climate. One of the most prominently discussed urban climate phenomena is the elevated temperature in cities compared to their rural surroundings, called the urban heat island (UHI) effect. Application of Local Climate Zones (LCZs) and eddy-covariance (EC) measurements above the urban canopy layer (UCL) currently miss fine scale differences within the UHI on a street canyon level, where citizens are exposed to environments of potentially increased heat stress. To improve the understanding of the UCL climate, this thesis aims at linking spatial high-resolution air temperature and humidity perturbation patterns with turbulent energy fluxes and a nonparametric compositional land use model within the UCL during the afternoon heat peak. To achieve this, a newly developed mobile EC system was installed onto a cargo bike, and three measurement rides were conducted in the northern “St Georgen/ Burg” district of the mid-sized central European city of Bayreuth. The measurement rides were done during the afternoon, sampling air temperature, vapor pressure, and wind at a frequency of 20 Hz. For the energy flux measurements, turbulent flow observations were corrected using an integrated high precision inertial navigation system and perturbation periods were fitted to calculate flux densities along approximately homogeneous street transects. Additionally, a network of eight microweatherstations (MWS) was setup along the measurement route to provide continuous observations of air temperature and solar radiation as five-minute averages. Two-minute stops were performed at each MWS to compare climate parameter measurements between the mobile and stationary measurement setups. The evaluations in this thesis were limited to days of observed autochthonous synoptic conditions, as these allow for locally influenced atmospheric patterns to form with minimal advective disturbance. In assessment of the spatial high-resolution perturbation patterns, the land use model could explain around 65 % of the humidity perturbations but lacked the complexity to achieve similar results for air temperature perturbations. These could be broadly explained by discussing the interactions of radiation and urban morphology. The EC-system showed promising results for mapping differing land use effects on the energy budget and provided insights into the processes shaping air temperature and humidity perturbation patterns. The applied land use model and mobile EC measurement method left room for improvement. Air temperature perturbations within the UCL of St Georgen/ Burg could only be assessed considering a variety of underlying processes. Correlation of air temperature perturbations with humidity perturbations was reduced within the city body due to a lack of available water for evapotranspirative heating reduction. Instead, angle dependent shading caused by high buildings was a prominent cause for cooler patches among the dryer parts of the city. Vegetation within the district could only lead to a significantly greater relative temperature reduction than the reduction achieved through shading in

dense patches of park-like structures. The continuous air temperature measurements could show that heat retention within the district during the late afternoon and night was linked to increased building densities. The results emphasised the importance of differentiated city planning in heat mitigation, that accounts for the complexity of the urban canopy layer heat island. The discussed forcings of heat accumulation like high shortwave absorptivity of dark impervious surfaces and heat retention through high thermal diffusivity of urban building materials can help reduce heat stress for citizens in future city planning. Application of identified possible mitigation strategies like land unsealing, preservation of dense vegetation patches and active consideration of shade casted by buildings, can be assessed in a cost-benefit evaluation based on their quantitative impacts discussed in this thesis. The newly developed methods can be applied for future investigations within the UCL after implementation of further improvements.

Table of contents

I. List of figures

II. List of tables

III. Glossary

Abreviations		Descriptions
EBG		Ecological botanical garden
EC		Eddy covariance
LCZ		Local climate zone
MWS		Microweatherstations
	AA	Allotment association
	CF	Correction facility
	GY	Graveyard
	LS	Leersstrasse
	RH	Retirement home
	SG	St Georgen
	TP	Tekirdağplatz
	WA	Wilhelminenaue
MobiFast		mobile measurement device used for this thesis
ToD		time of day

Symbols	Descriptions	Units
Bo	Bowen Ratio	[1]
$c(CO_2)$	concentration of CO_2 in the air	[mmol m^{-3}]
$c(H_2O)$	concentration of H_2O in the air	[mmol m^{-3}]
c_p	specific heat at constant pressure	[J kg^{-1} K^{-1}]
e	vapor pressure	[kPa]
h	height	[m]
$K\downarrow$	shortwave downward radiation or solar radiation	[W m^{-2}]
$K_{dir}\downarrow$	direct solar radiation	[W m^{-2}]
N	number or quantity	[1]
P_{atm}	atmospheric pressure	[kPa]
Pos	position data	[1]
p, r, h	pitch, roll, heading	[°]
q	specific humidity	[kg kg^{-1}]
$Q*$	net radiation	[W m^{-2}]
Q_B	ground heat flux	[W m^{-2}]
Q_E	latent heat flux	[W m^{-2}]
Q_F	anthropogenic heat	[W m^{-2}]

Q_H	sensible heat flux	[W m^{-2}]
R^2	coefficient of Determination	[1]
rH	relative humidity	[1]
RTK	real time kinetics	[m/° s$^{-1/-2}$]
T_{air}	air temperature	[°C/ K]
TKE	turbulent kinetic energy	[m^2 s^{-2}]
U	wind speed	[m s^{-1}]
U_{gust}	gust speed	[m s^{-1}]
u	wind speed, u-component (lateral)	[m s^{-1}]
u_{true}	wind speed, u-component after rotation into cardinal directions	[m s^{-1}]
v	wind speed, v-component (lateral)	[m s^{-1}]
v_{true}	wind speed, v -component after rotation into cardinal directions	[m s^{-1}]
w	wind speed, w-component (vertical)	[m s^{-1}]
$\overline{w}$	temporal mean wind speed, w-component (vertical)	[m s^{-1}]
w'	deviation from mean wind speed, w-component (vertical)	[m s^{-1}]
$\overline{w'x'}$	covariance of w and x	differing
x	scalar or vector	differing
$\bar{x}$	temporal mean scalar or vector	differing
x'	deviation from mean scalar or vector	differing
ΔQ_S	net heat storage change	[J; W m$^{—2/-3}$]
ΔQ_A	net heat advection	[J; W m$^{—2/-3}$]
λ	latent heat of vaporization of water	[J kg^{-1}]
ρ	air density	[kg m^{-3}]
φ	meteorologic wind direction	[°]
φ_{true}	meteorologic wind direction after rotation into cardinal directions	[°]

1 Introduction

1.1 Motivation

Cities in the mid latitudes can be expected to experience twice as intense heat stress compared to their rural surroundings by 2050 in context of anthropogenic climate change for all IPCC RCP scenarios (Dodman et al., 2022). In central Europe high temperatures are already associated with increased mortality rates in urban areas during the summer, as they pose additional microclimate-related stress onto vulnerable groups like individuals with pulmonary and cardiovascular diseases (Zhang et al., 2024). A comprehensive understanding of the climatic urban environment as living space for many central European citizens is therefore required to develop mitigation strategies and reduce future heat related health risks.

The phenomenon of higher temperatures in cities compared to their rural surrounding, known as the "urban heat island" (UHI) effect, has already been studied thoroughly to this day (Aslam and Rana, 2022; Oke et al., 2017; Bechtel et al., 2019). Since its first public description in the book "The climate of London" by Luke Howard in 1833 (Mills, 2008), the initial discrimination between the urban and rural sites as agents for UHI magnitude has been modified to account for more detailed differentiations of surface characteristics impacting the local climate. The concept of „Local climate zones" (LCZ's) presented by Stewart and Oke in 2012 was one conclusive approach to take a spectrum of land use types into account for UHI studies (Stewart and Oke, 2012). The applicability of LCZ's has been repeatedly documented for intra- and intercity comparisons (Aslam and Rana, 2022; Leconte et al., 2015; Cardoso and Amorim, M. C. C. T., 2018; Lehnerta et al., 2018). However, the concept was intrinsically designed to be limited to scales of several 100 meters per LCZ (Stewart and Oke, 2012), missing micro-scale temperature deviations in complex urban terrains (Rahmani and Sharifi, 2025; Quanz et al., 2018). To capture these micro-scale deviations, mobile measurement campaigns have emerged enabling to map instantaneous physical climate elements in high spatial resolution (Kousis et al., 2022). These measurements usually focus on climate elements in context of LCZs, often missing to quantify impacts of turbulent atmospheric energy fluxes and sub-LCZ differences in land use on climate elements.

This thesis aims at incorporating turbulent atmospheric energy fluxes and sub-LCZ land use characteristics into the evaluation of spatial high-resolution air temperature (T_{air}) and humidity perturbations. The focus is set on the afternoon heat peak during July and August, when thermal stress experienced by the citizens due to T_{air} is expected to be highest (Figure 2.3). The underlying mobile measurement campaign was conducted in the northern "St. Georgen/ Burg" district of the central European mid-sized city of Bayreuth. To this day, around 30 % of the German population live in mid-sized cities like Bayreuth (Bundesinstitut für Bau-, Stadt- und Raumforschung, 2023). The UHI effect has already

been documented for the city. Previous studies have investigated the city's broad scale response to heat waves (Sungur et al., 2025; Spaete, 2023), studied cold air advection (Tschuschke A., 2019; Schappacher, 2024), and quantified a park cool island in the city centre (Spies, 2019). Since 2018, Bayreuth is continuously equipped with a dense network of microweatherstations (MWS), initially installed as part of the MiSKOR project (Minderung Städtischer Klima- und OzonRisiken, 2018-2020) (Thomas and Samimi, 2021). In this network, the SG MWS location was already identified as one of the warmest spots in the city between September and March (Spies, 2019). To put the mobile measurements into context of the diurnal cycle, the network density was increased for the campaign, capturing several different land use types within the "St. Georgen/ Burg" district.

The main goal of this thesis is to identify and quantify spatial high-resolution T_{air} and humidity perturbation patterns within the urban canopy layer during the afternoon heat peak and determine their origin in the exchange of energy between atmosphere and urban surfaces as radiation and turbulent fluxes. Investigating these patterns and their origin can advance understanding of the micrometeorological processes within the urban canopy layer heat island in respect to urban structures.

The maps of T_{air} perturbation patterns created in the process of this thesis were used by an external commercial consultant company to identify hot spots in the St Georgen/ Burg district and support their development of a heat adaption strategy in collaboration with the city of Bayreuth (Stadt Bayreuth, 2025). The evaluations of complementary continuous night measurements and measurement rides performed during a radiation night were done by Sophie Resch in a complementary bachelor's thesis (Resch, 2025).

1.2 Theoretical foundations

1.2.1 Urban climate

The urban climate as a whole can be described as a mesoscale phenomenon caused by distinct morphologic and emissive features within a city that differ greatly from its surroundings (Oke et al., 2017). Areas covered with impervious materials, along with efficient drainage systems and a reduced vegetation cover, cause a reduction in water availability and thereby atmospheric humidity, most pronounced during the summer (Malberg, 2007). This reduction limits the possibilities of cooling by evapotranspiration during daytime. Reduced albedo of urban surfaces and increased heat diffusivity within the city body in combination with a partial trapping of radiation in street canyons can lead to increased warming and reduced cooling rates compared to rural surroundings, further strengthened by anthropogenic heat sources (Oke et al., 2017). The result is a higher mean air temperature within the city volume compared to its rural surroundings mostly observed during night (Oke et al., 2017). This so-called urban heat island (UHI) effect is

especially pronounced during calm and clear conditions (Malberg, 2007). It can be reduced and partially reversed during the day due to turbulent mixing as well as lower incoming shortwave radiation caused by building-induced shading and emission-induced aerosol absorptance (Oke et al., 2017). Aggregations of vegetation on pervious soils that are large enough can lead to an effect contrary to the UHI called the park cool island (PCI), usually defined for the nighttime (Oke et al., 2017). The accumulated heat in the city body reduces surface cooling rates via outgoing longwave radiation that is additionally trapped in street canyons. This also retains heat as increased T_{air} within the street canyons causing the strong UHI intensity during clear and calm nights. Starting point for assessing the mechanisms influencing urban climate properties in its complexity can be the energy budget. The three-dimensional structure within the city body and the presence of anthropogenic heat sources require some modifications to the one-dimensional surface energy balance equation used for flat homogenous surfaces. This one-dimensional energy balance equation of net radiative balance ($Q*$), sensible heat flux (Q_H), latent heat flux (Q_E) and ground heat flux (Q_B) is therefore expanded accounting for anthropogenic heat release (Q_F) and advective transport of energy (ΔQ_A) (Oke et al., 2017). As energy is not only exchanged with the upper ground but rather exchanged with and stored within the whole city body, the ground heat flux term is exchanged by the net storage change (ΔQ_S). The resulting formula describes the energy budget for a defined urban sub-volume (Equation 1.1).

$$Q* + Q_F = Q_H + Q_E + \Delta Q_S + \Delta Q_A \tag{1.1}$$

Due to anthropogenic emissions and heat-induced convection, an urban boundary layer forms above the city body that resembles a dome for calm conditions and a plume for moderate wind speeds (Oke et al., 2017). The lowest sublayer within that urban boundary layer is the urban canopy layer, located between the ground and rooftop level. It is subject to wind channelling effects and highly diverse radiation budgets, leading to the formation of distinct microclimates (Quanz et al., 2018). The urban canopy layer is the habitat for most urban citizens and will be the main focus of this thesis. Applying the urban energy budget formula to the urban canopy layer, the PCI can be expected to establish also during day under autochthonous conditions. Reduced solar radiation due to shading and missing anthropogenic heat sources, along with a dominating latent heat flux due to evapotranspiration and missing advection, can be expected to prevent heat accumulation.

1.2.2 Eddy covariance method

The eddy covariance (EC) method is a mathematical algorithm that enables calculation of vertical fluxes in the atmospheric boundary layer (Foken, 2017). It enables to reduce the exchange processes between atmosphere and surface to a one-dimensional mathematical problem (Aubinet et al., 2012). Due to this complexity reduction, it is only

applicable for homogeneous flat surfaces and during steady-state conditions (Foken, 2017). The EC method is based on the proportionality of vertical flux densities to the covariance of the vertical wind (w) and an additional scalar or vector (x) (Aubinet et al., 2012). Thereby it directly captures the vertical transport of energy, mass or momentum and does not require empirical coefficients (Foken, 2017). For determination of the covariance, w and x need to be decomposed into a mean component ($\overline{w}$ and $\bar{x}$) and its deviation (w' and x') for a defined time period. This operation is called the Reynold's decomposition (Equation 1.2a). Using this decomposition, a covariance ($\overline{w'x'}$) can be calculated for the defined perturbation time period with the respective number of observations (N) (Equation 1.2b).

$$w = \overline{w} + w'; \;\; x = \bar{x} + x' \tag{1.2a}$$

$$\overline{w'x'} = \frac{1}{N-1}\sum_{k=0}^{N-1}[(w_k - \overline{w_k}) * (x_k - \overline{x_k})] \tag{1.2b}$$

(Foken, 2017)

The determination of the perturbation time period is critical, as it acts as a high pass filter, for the measured turbulence spectrum, missing all turbulent low-frequency contributions with time scales longer than the chosen time period (Aubinet et al., 2012). However, the length of the time period is limited by the assumption of steady state conditions, which can usually only be met for time periods of up to 10-20 minutes in unstable stratification during summer days (Foken, 2017). An additional criterion for the applicability of the EC method is a negligible mean vertical wind, most commonly achieved by performing a double rotation of the reference coordinate system into the main streamlines for each time period (Foken, 2017). With the z-axis being orthogonal to the surface, the first rotation is a horizontal rotation around the z-axis, bringing the x-axis into the main streamline and reducing the mean lateral y-axis wind component to zero (Aubinet et al., 2012). The second rotation is performed around the new y-axis, reducing the mean vertical wind to zero (Aubinet et al., 2012).

The two fluxes exchanging energy with the surface via wind turbulence are the sensible and the latent heat flux. The sensible heat flux transfers enthalpy via heat of the air and is proportional to the covariance of air temperature T_{air} and vertical wind w. The latent heat flux transfers enthalpy via heat stored in evaporated water and is proportional to the covariance of specific humidity q and the vertical wind. To calculate the sensible heat flux, the buoyancy flux calculation can be used with the applied Schotanus correction (Equation 1.3). This equation uses the sonic temperature T_S, derived from the sound velocity in the sonic anemometer measurement path. EC measurements are usually performed using fast response sonic anemometers and optical gas analysers, to enable capturing the high-frequency part of the turbulence spectrum of up to 10-20 Hz (Foken, 2017). T_{air} can be calculated from T_S, by adjusting for the air density modification caused

by water vapor under usage of gas analyser vapor pressure (e) and atmospheric pressure (p) data (Equation 1.4). Additionally, the air density (ρ), specific heat at constant pressure (c_p), latent heat of vaporization of water (λ) and Bowen ratio (Bo) are needed.

$$Q_H = \overline{w'T'}\rho c_p = \rho c_p \frac{\overline{w'T_S'}}{1+0.51\frac{\overline{T_{air}}c_p}{\lambda Bo}} \tag{1.3}$$

(Schotanus et al., 1983)

$$T\,[K] = \frac{T_S\,[K]}{1 + 0.32 * \frac{e[kPa]}{p[kPa]}} \tag{1.4}$$

(Kaimal and Gaynor, 1991)

$$Q_E = \overline{q'w'}\rho\lambda \tag{1.5}$$

(Aubinet et al., 2012)

For calculation of the latent heat flux, the specific humidity q can be used (Equation 1.5). To account for errors due to constant convective humidity fluxes and density fluctuations, the WPL-correction can be applied (Webb et al., 1980). To correct underestimation of the energy fluxes in the high frequency range caused by the sensor separation and the path length, the correction method by Moore is usually applied (Moore, 1986). Lastly, the Reynold's decomposition can also be used to calculate the turbulent kinetic energy (TKE) as a measure of turbulence intensity (Equation 1.6). The TKE represents the kinetic energy contained in turbulent flows. This kinetic energy is needed to enable the turbulent energy fluxes.

$$TKE = 0.5(\overline{u'^2} + \overline{v'^2} + \overline{w'^2}) \tag{1.6}$$

(Foken, 2017)

1.3 Research questions and hypotheses

To achieve the goal defined at the end of chapter 1.1 in consideration of the underlying processes described in chapter 1.2, the following research questions and hypotheses were formulated:

Research Question 1: What are the spatial patterns of **air temperature** and **absolute humidity** within the St. Georgen/Burg neighbourhood during autochthonous conditions and can **land use** maps help **explaining** these patterns?

Hypothesis 1a: During the summer, the **land use distribution** is a strong **predictor** for spatial urban canopy layer **air temperature** and **absolute humidity** differences during autochthonous synoptic conditions. For these conditions, an increase in the proportion of land covered by **buildings** and **pavement** compared to vegetation is **associated with higher air temperatures** and **lower absolute humidity**. These existing temperature differences increase during the late afternoon transition.

Hypothesis 1b: Due to a lack of buildings as heat storage as well as shading and evapotranspirative heating reduction during the day, the formation of a **park cool island** is expected in the **graveyard** southern meadow and the **allotment association** during autochthonous synoptic conditions throughout day and night.

Research question 2: What are the spatial patterns of sensible and latent heat flux densities in the St. Georgen/Burg neighbourhood during the afternoon air temperature peak?

Hypothesis 2a: For autochthonous afternoons in the summer, the **upward sensible heat flux** in the urban canopy layer is **increased** for higher proportions of land covered by **buildings** and **pavement** compared to vegetation. Therefore, it is expected to be **highest** for **densely built** main streets, **lower** for **residential areas** and **lowest** for rural **grassland/meadows**.

Hypothesis 2b: Upward **latent heat flux** is **limited** by the amount of surrounding **vegetation** or open **water** and is therefore expected to be **highest** in the rural **floodplain** meadow of the Wilhelminenaue. It is also significantly increased at the **graveyard** southern meadow bikeway and the **allotment association**.

2 Methods

To investigate the formulated research questions and hypotheses, data is used from a measurement campaign conducted during July and August of 2024 in the northeast of Bayreuth, Germany. Continuous stationary observations were made at eight measurement locations for the whole two months using microweatherstations (MWS) (Figure 2.1). Three measurement rides were performed using an instrumented cargo bike. They took place in the afternoon during "heat days", defined by the DWD as days with a maximum temperature of at least 30 °C (DWD, 2025a). The continuous stationary observations served for investigating larger-scale spatial patterns in the diurnal course. The objective for the mobile measurements was to sample representative fine scale perturbations of T_{air} and vapor pressure (e) as well as turbulent sensible and latent heat fluxes to identify spatial patterns caused by surrounding land use characteristics.

2.1 Research site

Bayreuth is a mid-sized city with an elevation of around 345 m above mean sea level, located in a valley in the northeast of Bavaria (49° 56' 46" N, 11° 34' 44" E), the southeasternmost state of Germany (Figure 2.1). It currently covers an area of around 67 km^2 and has close to 75,000 inhabitants. Due to its location in a transition zone between maritime and continental climate, Bayreuth experiences a reduced precipitation. For the period of 1991-2020, the mean precipitation was at 718 mm in the ecological botanical garden (EBG), 73 mm below the average across Germany (DWD, 2025b; Thomas, 2025). During the summer of 2024 the mean T_{air} in the EBG was 0.8 °C/ 2.6 °C higher in July/ August than for the reference period of 1991-2020 (Thomas, 2025).

Table 2.1: Names and locations of the eight MWS and the EBG measurement site. North and east coordinates are supplied in the Projection "UTM Zone 32N EPSG: 25832", in line with Figure 2.1.

Name	North	East	Surroundings
Retirement home (RH)	5537225	685851	Retirement home next to a construction site at the edge of the district adjacent to a lower main road
Leersstrasse (LS)	5536998	686150	Residential area with detached apartment buildings
Allotment association (AA)	5536906	685261	Gardens crossed by a bike-/walkway, adjacent to the train tracks in the northwest
Correction facility (CF)	5536877	685456	Border between the correction facility backyard and cropland at the northwestern edge of the district
St Georgen street (SG)	5536734	685933	Densely built main street within the district without treeline
Graveyard (GY)	5536446	685999	Meadow south of the graveyard, adjacent to a treelined bikeway
Tekirdağplatz (TP)	5536423	685591	Square at the extension of the downhill SG street with treeline
Wilhelminenaue (WA) – rural reference	5535915	686363	Bikeway in a floodplain valley meadow, slightly elevated spot
Ecological botanical garden (EBG) – rural reference	5533461	685619	Meadow within the ecological botanical garden (EBG) partly surrounded by trees, close to a pond

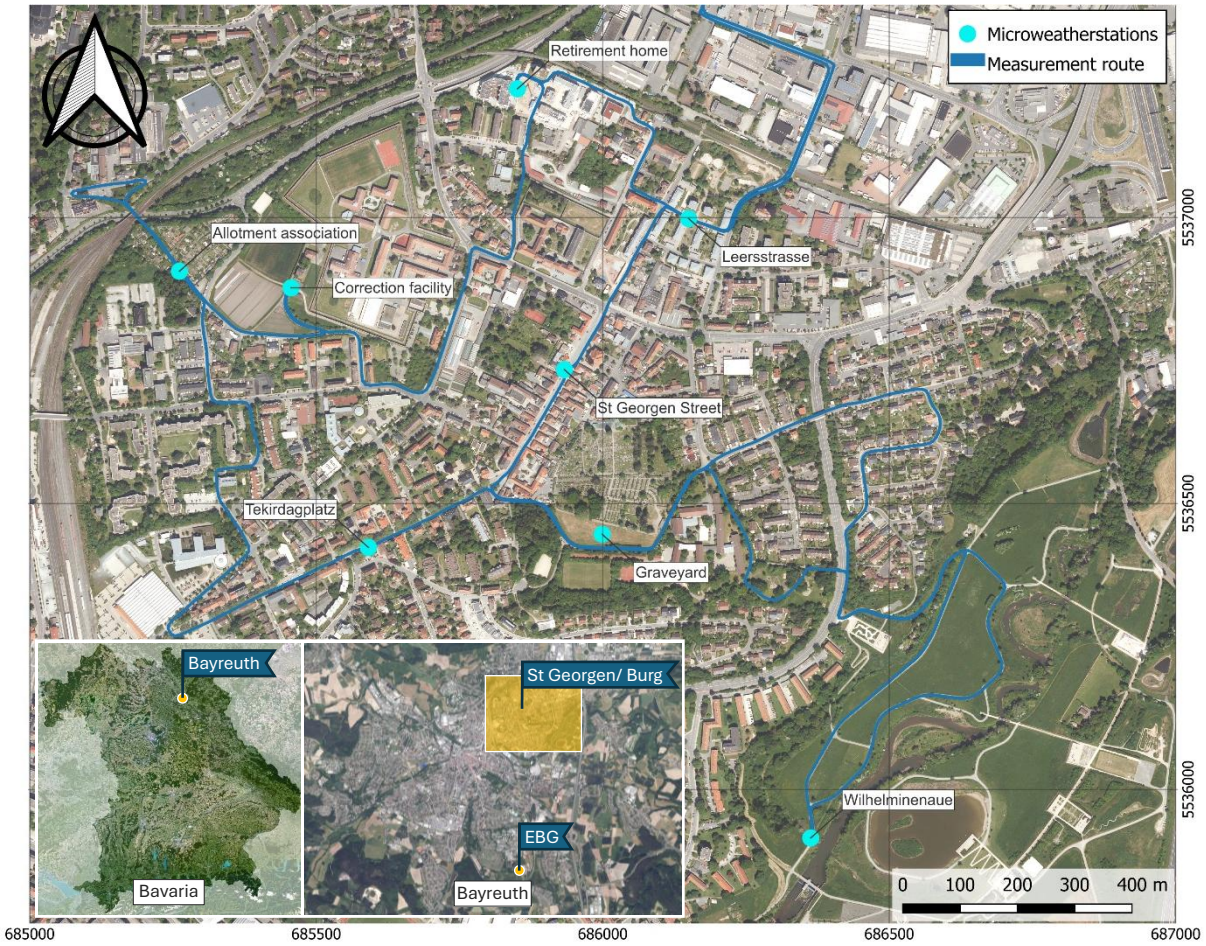

Figure 2.1: Orthophoto of the research site "St. Georgen/ Burg" in Bayreuth. The route (dark blue) for the mobile measurement campaign was followed counterclockwise. 2-minute stops were performed along the route right next to the MWS (light blue). In the lower left corner, the location of Bayreuth in Bavaria (left) and the research site "St Georgen/ Burg" as well as the rural reference "ecological botanical garden" (EBG) within Bayreuth (right) can be found. Exact coordinates of the MWS and a brief description of their surroundings is listed in Table 2.1. (Maps: Bayerische Vermessungsverwaltung 2025, Route and MWS were added in QGIS, Projection: UTM Zone 32N EPSG: 25832)

2.2 Data acquisition and materials

2.2.1 Measurement devices

For continuous measurements of the urban canopy layer weather elements, two MWS were used from the previous "MiSKOR" project (Thomas and Samimi, 2021) and six were additionally positioned along the measurement route (Figure 2.1). Five of the stations were set up for the first time, the graveyard (GY) station was removed from its former location in the MiSKOR network and repositioned. The MWS were installed on streetlamp posts at a height of 3.50 m above ground. The GY station was installed on a mast in 2.50 m height. Measurements from a meteorology mast in the ecological botanical garden (EBG) were used as additional rural reference. The exact locations, along with a short description of the surroundings can be found in Table 2.1. The six additionally setup MWS were previously tested for four whole days in June 2024 in the EBG next to the meteorology

mast equipped with a temperature and humidity probe (HMP 45, Vaisala, Vantaa, Finland) (Figure 2.11). The test results are discussed at the end chapter 2. During the two-months measurement period, data observed by the MWS (ATMOS 41, METER Group, Pullman, Washington, USA) was logged in real time via mobile telecommunications using dataloggers (EM60G, METER Group, Pullman, Washington, USA). Additionally, the Mistel and Kaemmerei MiSKOR stations were used for synoptic classification. Details for these stations' surroundings can be found in Schappacher, 2024.

For detecting fine scale perturbations of T_{air} and e along with wind vectors, as well as turbulent atmospheric energy fluxes, a mobile eddy covariance system was built. It consisted of an ultrasonic anemometer (uSonic-3 Cage MP, METEK, Elmshorn, Germany), an open path infrared gas analyzer (SmartFlux 3, LI-COR, Lincoln, NE, USA), an inertial navigation system (Ellipse-D INS, SBG systems, Carrières-sur-Seine, Île-de-France, France) and a laptop installed to a triangle truss on top of a cushioned steel plate. The whole setup was fastened onto the front platform of a cargo bike. The equipped cargo bike will from here on be called "MobiFast". Anemometer and gas analyzer data was logged using the SmartFLux3 system, while the motion data was logged using the sbgDataLogger tool provided by the inertial navigation system (INS) manufacturer. Both used a sample frequency of 20 Hz and were operated using the installed laptop. Since both systems aligned their system time with UTC time via the global navigation satellite system (GNSS) antennas, the 20 Hz data of both systems could later be synchronized by timestamp. The sonic anemometer north orientation and the INS x-axis were installed facing forward to ease calculation of true wind directions. For the eddy covariance measurements, the gas analyzer was mounted downwind below the sonic anemometer.

For stationary and mobile measurements, the device names and details on the measurement parameters are listed in Table 2.2. Pictures of the measurement setups can be seen in Figure 2.2. The tags in Figure 2.2 correspond to the tag numbers in Table 2.2.

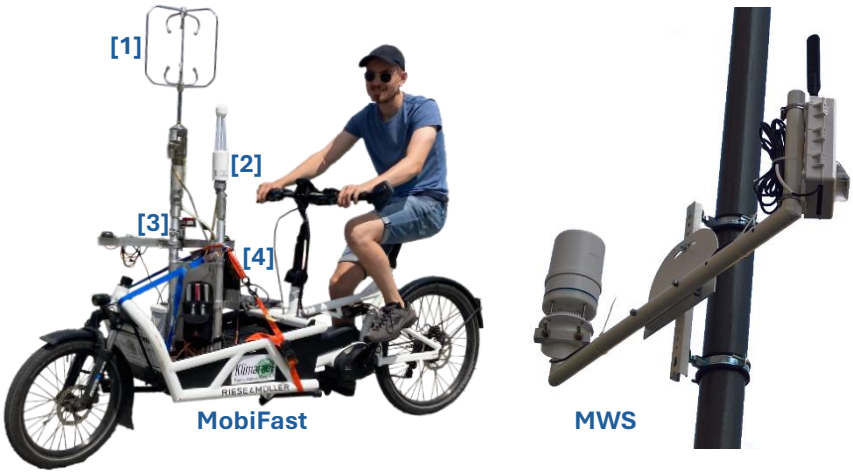

Figure 2.2: Measurement setup for the mobile measurements (left) and the MWS (right). The mobiFast system consisted of: [1] Ultrasonic anemometer, [2] open path infrared gas analyzer with Smart flux logging system, [3] inertial navigation system, [4] Laptop. (Pictures: Sophie Resch (left), Dr. habil. Johanner Lüers (right))

Table 2.2: Table of devices used for the data acquisition, the sampled weather elements (WE), units, measurement frequency (Freq) and aggregation interval (Agg), measurement height (MM height) and tag in Figure 2.2.

Device name	WE	Unit	Freq/Agg	MM Height	Tag
METEK sonic anemometer, uSonic-3 cage multipath	T_S	°C	20 Hz	1.60 m	MobiFast 1
	u, v, w	m s^{-1}			
Licor Open Path LI-7500DS infrared gas analyzer with SmartFLux3 System	$c(H_2O)$	mmol m^{-3}	20 Hz	1.35 m	MobiFast 2
	$c(CO_2)$	mmol m^{-3}			
	P_{atm}	kPa			
SBG Ellipse-D RTK INS with dual antenna	Pos	° N, E	20 Hz	1.10 m	MobiFast 3
	p, r, h	°			
	RTK	m, ° $s^{-1, -2}$			
ATMOS 41 Microweatherstations (MWS)	$K\downarrow$	W m^{-2}	0.1 Hz/ 5 min avg	3.5 m	MWS
	T_{air}	°C			
	rH	%			
	e				
	φ	°			
	U	m s^{-1}			
	U_{gust}	m s^{-1}	5 min max		
HMP 45	T_{air}	°C	0.1 Hz/ 10 min avg	2 m	EBG
	rH	%			
UTK SDE Sunshine sensor	$K\downarrow$	W m^{-2}	0.1 Hz/ 10 min avg		
	$K_{dir}\downarrow$	W m^{-2}			

2.2.2 Measurement rides

The roughly 10 km long measurement route included the St. Georgen/ Burg district and the adjacent flood plain meadow "Wilhelminenaue" (Figure 2.1). Measurement rides were conducted on three days of autochthonous synoptic conditions. The rides took place on the 30th of July 16:12-17:00, 12th of August 16:19-17:30 and the 14th of August 17:00-18:15 CEST to cover the expected time of the afternoon heat peak, determined in Figure 2.3. Two-minute stops were performed along the route, next to each of the eight MWS locations to compare temperature and humidity measurements between MobiFast and the MWS. This also allowed for comparison between mobile and stationary flux measurements. Before starting, figure-eight loops were ridden to initialise the INS system. The SBG Ellipse-D possesses an internal "Extended Kalman Filter" to align the internal motion unit (IMU) with a sample frequency of 200 Hz to the GNSS signals, coming in at a rate of 1 Hz. The measurement ride began, as soon as the Kalman filter was aligned. Start and end point was the BayCEER building northeast of the St Georgen/ Burg district. The route was followed counterclockwise from the LS MWS as first and last stop of the measurement ride.

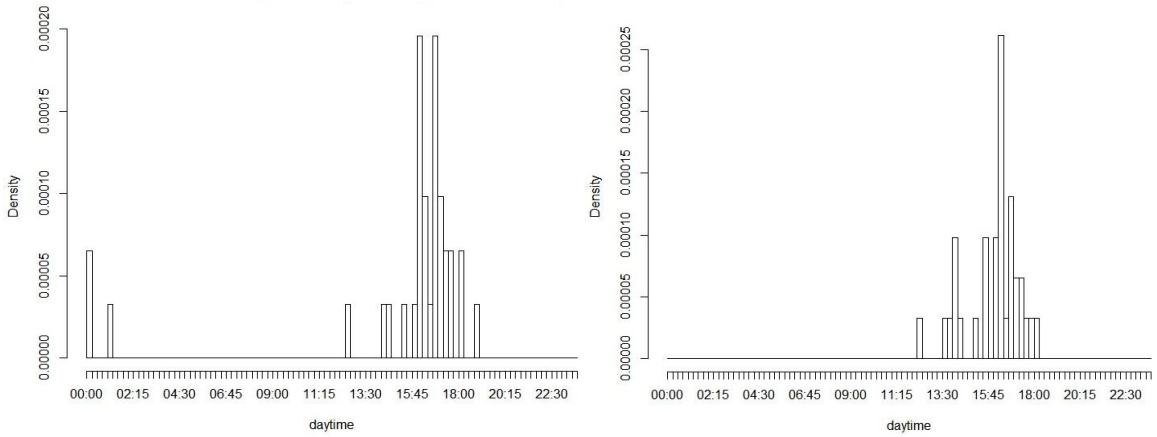

Figure 2.3: Histogram of daytime when maximum temperatures were measured during July (left) and August (right) 2022 at the St. Georgen street MWS. The highest density of measured temperature maxima is seen around 16:00-16:15 and 16:45-17:00 in July and 16:15-16:30 in August. This graph was the orientation for setting the time period for the mobile measurement rides. Due to a prolonged initialization of the MobiFast system on the 14th of August 2024, this days ride started with a 45 minutes delay.

2.2.3 Land use classification

To identify land use characteristics around the eight MWS and investigate the influence of surrounding land use on the spatial patterns of T_{air}, e and turbulent energy flux densities for the measurement rides, a polygon land use map was used (Figure 2.4). The map was provided by the State Institute for Geodesy of Bavaria and altered for usage in PALM-4 U by (Sungur, 2021; Sungur et al., 2025). As preparation, some land use types were aggregated into more general land use classes. The goal was to reduce the bias caused by distinct land use type occurrences in single locations. These could lead to correlations between site specific characteristics and a unique land use type that are caused by other site-specific characteristics. The following reclassifications were performed:

- “asphalt”, “cobblestone”, “paving stones” and “concrete” areas were classified as “solid pavement”
- “fine gravel”, “gravel” and “pebble stone” areas were classified as “loose pavement”
- “Deciduous broadleaf trees” and “evergreen needleleaf trees” areas were classified as “trees”
- “pond” and “river” areas were classified as “water”

Additionally, a layer of building areas was added. Bridges as “buildings” were removed and the building areas were stamped into the land use map, replacing other land use types within their area. The buildings will from here on be handled as an additional land use type. Since the map only captures trees in defined tree-dominated areas and misses trees located within other land use areas, a single-trees layer was additionally used. Both added map layers were also provided by the State Institute for Geodesy of Bavaria (Bayerische Vermessungsverwaltung, 2025). The land use map was used as this for

interpreting the continuous stationary measurements (Figure 2.4). Further changes and usage of the land use map for the mobile measurements are described in chapter 2.3. All map related processing was done using QGIS 3.34.10.

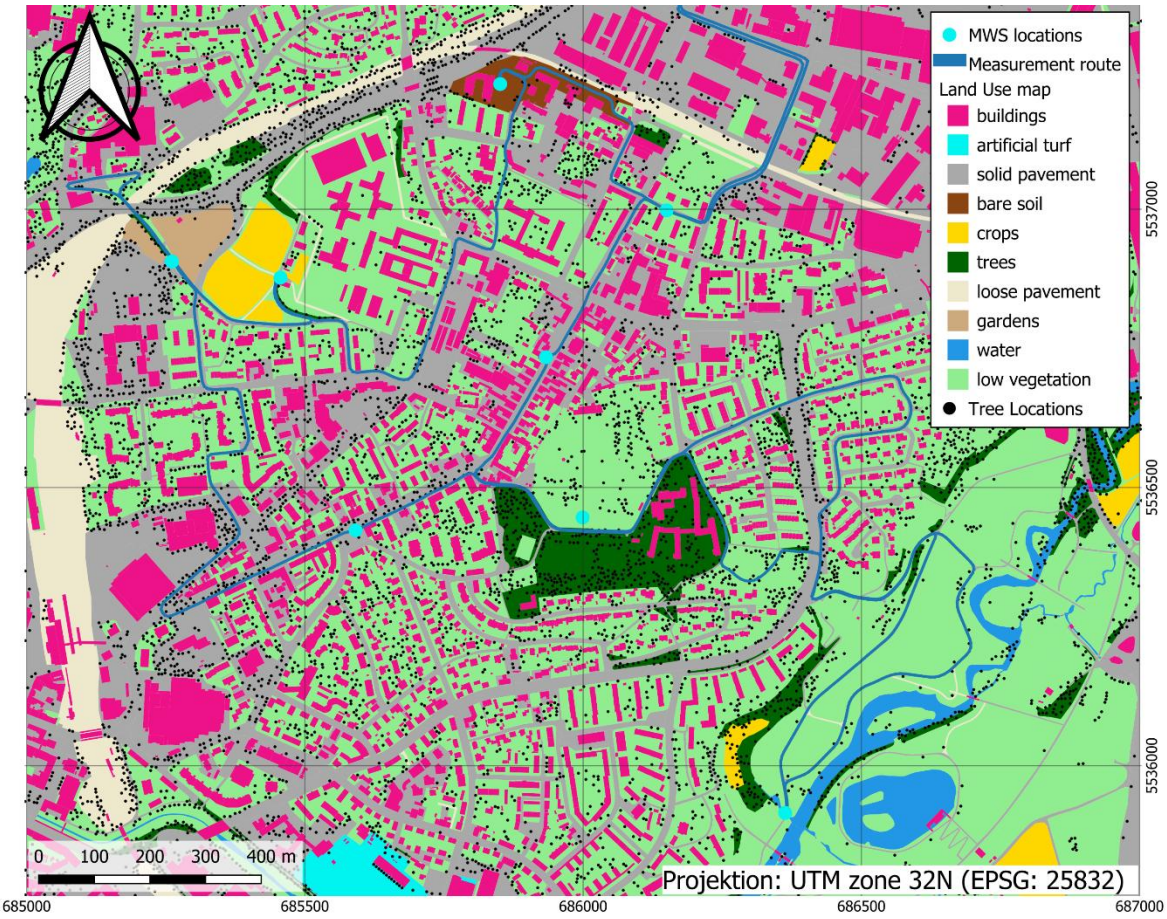

Figure 2.4 Map of the land use distribution within the research site including the mobile measurement route and the eight MWS locations. Tree locations, building areas and land use types were provided by the State Institute for Geodesy of Bavaria (Bayerische Vermessungsverwaltung, 2025).

2.3 Data processing and evaluation

2.3.1 Synoptic classification

Since the focus of this thesis is to investigate the effects of local land use characteristics on climate elements and flux densities, only measurements during autochthonous synoptic conditions will be considered. Autochthonous conditions apply when the state of the atmosphere in a location is determined by regional or local influences (DWD, 2025b). In this thesis the term is used to describe time periods of low wind velocities and reduced cloud cover. Low wind velocities result in a minimized air mass advection preventing strong mixing and reallocation of locally influenced air masses. A reduced cloud cover allows for high energy input due to shortwave radiation during the day, creating distinct microclimates dependant on albedo, water availability and shading under low wind conditions. The autochthonous time periods as described here, can be

expected to show the largest spatial temperature differences between areas of different land use in the urban context (Malberg, 2007).

For evaluation of the continuous stationary observations, first sunrise and sunset were classified. The sunset was the first datetime timestep after which the global radiation at the Mistel station was consistently below 10 W m^{-2} for at least 1 h. The sunrise was the last datetime timestep before which the global radiation at the Mistel station was consistently below 10 W m^{-2} for at least 1 h. A day was classified as autochthonous if it fulfilled the following three criteria:

- Direct radiation had a share of at least 80% on the global radiation for at least 46% of the time between 3 h after sunrise and 1 h before sunset at the EBG station (Figure 2.5)
- Gust speed was below 2.2 m s^{-2} for at least 53% of the time between 1 h after sunrise and 1 h before sunset at the Wilhelminenaue (WA)
- Radiation night conditions were fulfilled for at least 60 % of the time between sunset and 5 h before sunrise in the following night (compare Figure 8.11). Radiation night conditions were defined for conditions when the T_{air}-difference between the Mistel and Kaemmerei MWS was at least 2 K and U_{Gust} at the Mistel was below 2.2 m s^{-1}. This definition was adopted from Schappacher, 2024

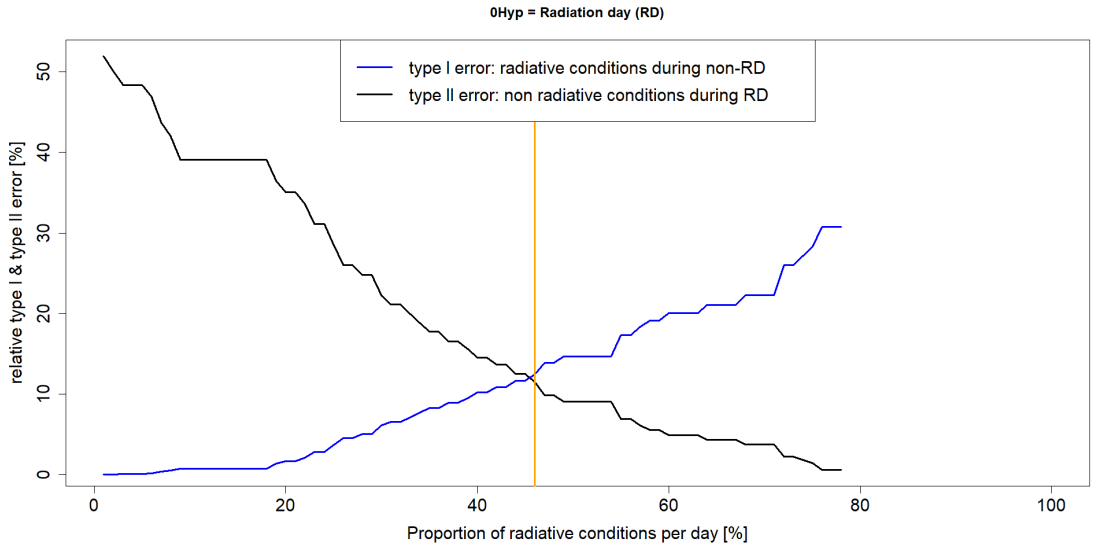

Figure 2.5: Proportion of the type I and type II error in classification of radiation days. The x-axis represents the threshold values for classification. The optimal classification threshold is marked by the vertical orange line. The corresponding plots for the other two criteria can be seen in the appendix as Figure 8.1.

The threshold values correspond to the decision boundaries for daily classification at which the shares of Type I and Type II errors for individual data points per day are equal. The daytime margins were narrowed in the first two criteria to avoid capturing conditions during transition times. Especially the start of the radiation criterion was shifted since the EBG station is shaded in the early morning (Figure 3.16). The radiation-night criterion was adjusted to end earlier since the nighttime data will only be evaluated until midnight in

this thesis. Nine days were classified as autochthonous during the measurement period in July and August.

2.3.2 Preparation of mobile data

All MobiFast datasets were processed using the bmmflux software created by Christoph K. Thomas before further usage:

The INS and SmartFlux data files were matched based on timestamp. The velocity data measured by the INS was used to subtract all movement velocities from the respective wind vectors. For evaluation of the temperature, humidity and wind vector data, 2 s block means of all 20 Hz values were calculated. Additionally, the water vapor concentration recorded in mmol m^{-3} was converted into vapor pressure (e) in bmmflux. For evaluation of the T_{air} perturbation, T_{air} was calculated from T_S using the formula by Kaimal and Gaynor (1991) (Equation 2.1).

$$T_{air}\,[K] = \frac{T_S\,[K]}{1+0.32*\frac{e[kPa]}{p[kPa]}} \tag{2.1}$$

(Kaimal and Gaynor, 1991)

For calculating the wind vectors during the measurement ride, first the wind direction was corrected to the true wind direction (φ_{true}) by adding the INS heading (h) to the measured wind direction (φ). The wind direction was previously retrieved from the measured two horizontal wind vectors in bmmflux (Equation 2.2).

$$\varphi_{true} = modulo(\frac{\varphi+h}{360}) \tag{2.2}$$

The corrected wind direction along with the wind speed (U), also calculated in bmmflux, was then transformed into a wind vector of an x- and y-component (u_{true} and v_{true}) (Equations 2.3a, 2.3b). Finally, the wind vectors were averaged from 2 s resolution to 4 s resolution to reduce noise in the wind vector maps.

x-component: $$u_{true} = U * \sin\left(modulo\left(\frac{\varphi_{true}+180}{360}\right) * \frac{pi}{180}\right) \tag{2.3a}$$

y-component: $$v_{true} = U * \cos\left(modulo\left(\frac{\varphi_{true}+180}{360}\right) * \frac{pi}{180}\right) \tag{2.3b}$$

2.3.3 Correction of instationarity and stochasticity

To enable a clean spatial comparison of T_{air} and e perturbations, the time instationarity experienced during the measurement rides needs to be compensated. This instationarity is caused by the ongoing diurnal progression, effecting the measurements taken only for spatial comparison in space and time. The correction process was applied to T_{air} and e using the eight main MWS except for the GY and Tekirdağplatz (TP). The GY station was

located on an unshaded meadow while the bike stop was done on the southerly adjacent, shaded bikeway. This would lead to misclassification of the actual instationarity in direct proximity of the measurement point when using the GY MWS. The TP station was only put up at the beginning of August and was left out to prevent errors in the intercomparison of the July and August measurement rides. The St Georgen street (SG) humidity measurements and the WA humidity and T_{air} measurements were later found to be flawed concerning their absolute values. Since the instationarity correction only operates with relative temporal perturbations within one hour, the errors were assumed to be negligible. Also, the influence of stochastic effects like cars and pedestrians passing close to MobiFast need to be reduced. This was achieved by spatial averaging under the assumption that the perturbations of T_{air} and e are indifferent to the absolute value. Tschuschke could confirm this assumption for T_{air} in a previous study (Tschuschke A., 2019). A list of instructions was developed and used for the instationarity and stochasticity correction process. With $\bar{X}$ as the temporal and $\hat{X}$ as the spatial mean of a value X, X_{rel} as a relative and X_w as the distance weighted X-value, d as distance, $M_{i,t}$ as a MWS value at a certain location and at a certain point in time, m_j as a MobiFast value at a certain location along the measurement route and t_{stop} as time frame of the 2-minute stop at the MWS, the following list of instructions was used:

I. Calculate MWS values for the whole ride relative to the 17:00 CEST value (Equation 2.4)

$$M_{rel,i,t} = M_{i,t} - M_{i,17:00} \tag{2.4}$$

II. Interpolate these relative values by nearest neighbour from 5-minute mean values to 2-second resolution values (Figure 2.6)

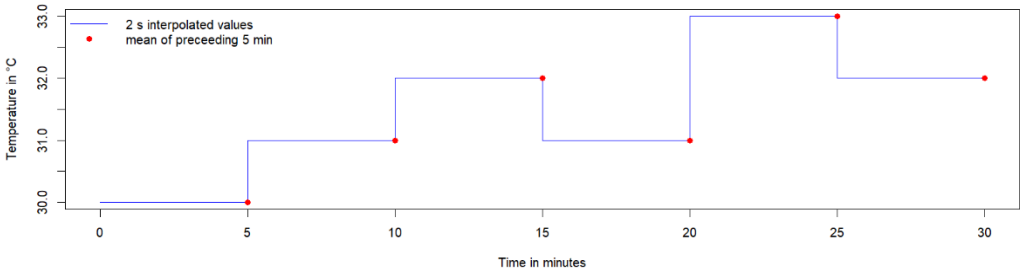

Figure 2.6: Example figure for the nearest neighbour interpolation.

III. Calculate the inverse squared distance weighted mean MWS value for each timestep and subtract it from the respective MobiFast measurement value (Equation 2.5, Figure 2.7)

$$w_{i,t} = \frac{1}{d_{i,j,t}^2};\ M_{rel_w,j} = \frac{\sum(w_{i,t} * M_{rel,i,t})}{\sum w_{i,t}} \rightarrow\ m_{w,j} = m_j - M_{rel_w,j,t} \tag{2.5}$$

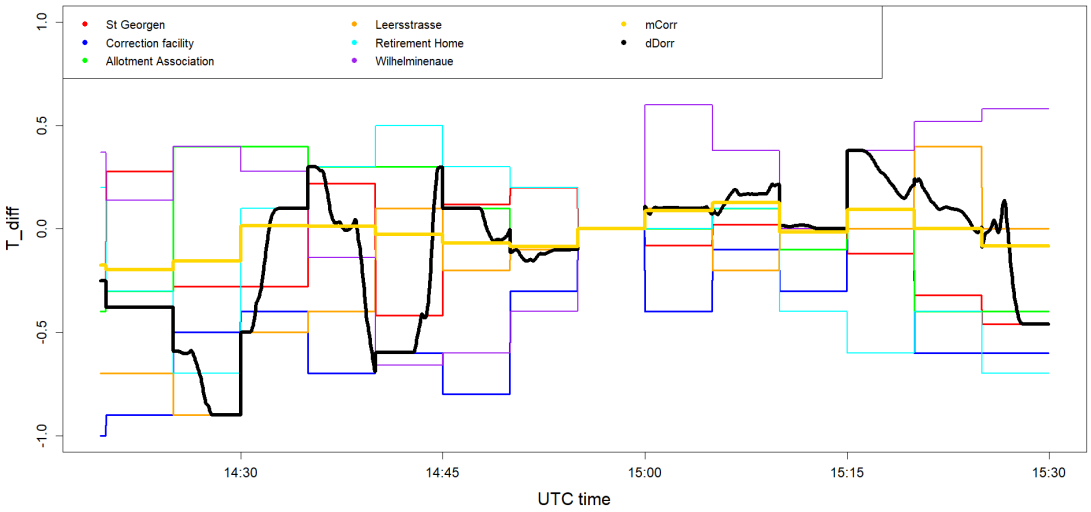

Figure 2.7: Relative T_{air} (T_diff) of the six MWS, the mean of all relative values (mCorr) and the inverse squared distance weighted mean (dCorr) for the 12th of August. The dCorr value corresponds to $m_{w,j}$ in III.

IV. Calculate the mean bias of all MWS (M_{bias}) relative to the respective mean MobiFast value during the 2-minute stops ($\overline{m}_{j,t_{stop}}$). Subtract that mean bias from the mean of the 17:00 MWS data ($\widehat{M}_{17:00}$) for every measurement ride (Equation 2.6)

$$M_{bias} = (\widehat{M_{\iota,t_{stop}} - \overline{m}_{J,t_{stop}}}) \mid for\ i \approx j\ ;\ M_{17:00,B_{corr}} = \widehat{M}_{17:00} - M_{bias} \qquad (2.6)$$

V. Subtract the bias corrected mean of all MWS values at 17:00 ($M_{17:00,B_{corr}}$) from the distance weighted MobiFast values of the respective measurement ride (Equation 2.7)

$$m_{w,rel,j} = m_{w,j} - M_{17:00,B_{corr}} \qquad (2.7)$$

VI. For each point every 10 m along the measurement route, calculate a mean of all bias corrected relative values within a 7.50 m radius ($m_{w,rel,j_{def}}$) (Equation 2.8)

$$m_{w,rel,j_{def}} = \hat{m}_{w,rel,j,t_{date}} \qquad (2.8)$$

VII. Correct for height (h_j) differences relative to the median height (h_m) using the dry adiabatic lapse rate of 9.8 K km^{-1} (Equation 2.9)

$$m_{w,rel,j_{def},h_{corr}} = m_{w,rel,j_{def}} - (h_m - h_j) * 9.8\ \mathrm{K\ km^{-1}} \qquad (2.9)$$

This way all measurement ride sections represented in the further evaluation also have the same weight. The maps produced using this procedure can be found in chapter 3.2. The values seen there correspond to $m_{w,rel,j_{def},h_{corr}}$: The height corrected spatial mean of a distance weight adjusted relative value for a certain circular area along the measurement route including all three measurement rides.

2.3.4 Eddy covariance flux measurements

For determination of sensible and latent heat flux densities, the eddy covariance (EC) method was used according to the basic principles described in chapter 1.2. The perturbation time scale was limited due to the high instationarity of the surroundings during the measurement rides. To ensure nearly steady-state conditions were fulfilled, the perturbation time periods were fitted to calculate flux densities along approximately homogeneous street transects. The net advection was assured to be negligible by using the coordinate rotation described in chapter 1.2.

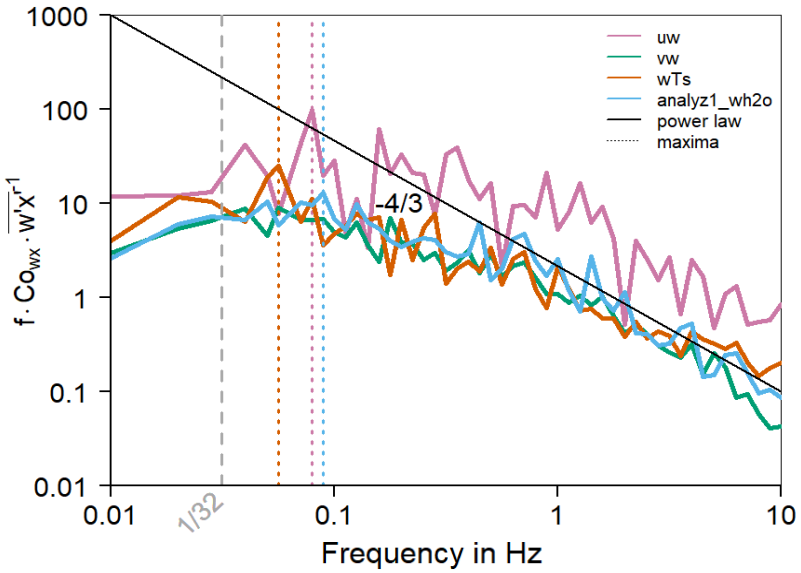

Figure 2.8: Mean frequency spectrum for the covariances of the three measurement rides. A perturbation time period of 52 seconds was used. The co-spectra calculation was done using Fast Fourier Transformation in bmmflux. The spectra were normalized by dividing by the mean covariance and multiplying the frequency. The chosen perturbation time period for this thesis is marked in grey.

This allowed for applying the EC method in the urban canopy layer. As the bike velocity of 4 to 6 m s^{-1} only allows for relatively short perturbation time periods of up to a minute in the heterogenous environment, only the high-frequency fraction of the turbulence spectrum could be quantified. Assuming a similar distribution of the inertial subrange turbulence across the research area, this choice still allowed for comparison of the fluxes along the route. A universal perturbation time period of 32 s was chosen as it was short enough to fit several homogeneous street transects and included the spectral maxima for the whole frequency spectrum of the three measurement rides (Figure 2.8). Moore correction and WPL correction were applied in the bmmflux calculations as well. Flux values were only used if the frequency correction factor of the Moore correction was below 1.5.

2.3.5 Land use correlations

The land use map seen in Figure 2.4 was used to attribute certain land use characteristics to the MWS and MobiFast measurement locations. To determine the area of surface influence around each measurement point, the concept of internal boundary layers was used. For horizontal advective conditions, an internal boundary layer forms downwind from a sudden change in surface properties like e.g. roughness (Foken, 2017). The height z_{IBL} of this internal boundary layer is proportional to the square root of the distance x to the surface roughness change (Equation 2.10).

$$z_{IBL} = 0.3 * \sqrt{x} \tag{2.10}$$

(Raabe and Foken, 2003)

Within the new equilibrium layer which forms under the internal boundary layer, the atmospheric conditions are impacted by the new surface properties (Foken, 2017). The internal boundary layer height within the study area was estimated to be at the measurement height of the MWS, since these are roughly at the height of the urban canopy layer boundary. The area of influence was determined to be a circle with a radius of x. With the same measurement hight of 3.50 m, this determination is in par with the previous studies using the MiSKOR network in Bayreuth done by Sungur and Spaete (Spaete, 2023; Sungur, 2021; Sungur et al., 2025). Therefore, the radius for the area of influence around the MWS amounts to 136 m (Equation 2.11).

$$x = (\frac{z_{IBL}}{0.3})^2 = 136\,m \tag{2.11}$$

The land use types around the MWS within this radius were gathered as shares within the circle area. The number of trees was sampled as trees per ha. Since the GY station was installed at 2.50 m above ground level, its radius amounted to 69.4 m.

For comparison of the stationary and mobile measurements, the same method was also used to determine the area of surface influence around the mobile measurement locations. With a measurement height of 1.60 m, the distance x amounted to 28.4 m. Since parts of the measurements were done while moving, the calculated distance value was applied as distance to a straight line along the measurement route for calculating the area of surface influence. The line for each measurement point was determined as the direct connection between the two centre points in-between a direct connection of the current data point to the previous and the next (Figure 2.9).

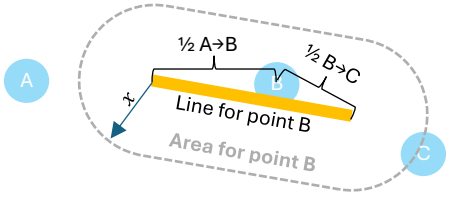

Figure 2.9: Example for the determination of the area around "point B"

To analyse the correlations between land use and the weather elements of T_{air} and e, the share of each land use type in the previously determined area around every measurement point or line was calculated for each individual ride. The values were then aggregated as spatial means along with the values of T_{air} and e as described in "Correction of instationarity and stochasticity". The land use types used for the MobiFast evaluation were aggregated further to avoid single site occurrence of individual land use types for the later conducted linear define. The following aggregations were made:

- "Solid pavement", "loose pavement" and "bare soil" were classified as "pavement", because "loose pavement" was predominantly present in the WA and "bare soil" was only present around the retirement home (RH)
- "Low vegetation" and "crops" were both classified as "low vegetation", because crops were only present around the correction facility (CF)
- "trees" and "gardens" were classified as "high vegetation" as "gardens" were only present at the allotment association (AA)
- "water" was left as a single land use type even though it only occurs in the WA. It is not expected to show random correlations due to single occurrence in the evaluation but to have an actual cooling effect on its surroundings that would be missed in aggregation with other land use types

Afterwards, several multiple linear regression models were fitted to investigate the explanatory power of the land use distribution for the measured spatial T_{air} and e perturbations. Since the land use type area share values are compositional variables, one value was left out as a reference variable to avoid multicollinearity. Multicollinearity can be caused by the inherent mutual dependency among compositional predictor variables, since each component can be expressed as the difference between the constant sum and the remaining variables (Valle et al., 2024). The land use type left out for this investigation was the building area as it is present for the most part of the route except for the WA. Secondary multicollinearity effects due to the reference variable being zero should therefore be minimal. For interpretation of the linear regressions, this method holds one important constraint: The response of the atmospheric dependant variable to an increase of a certain land use type share in the model, is always associated with an equal decrease of the reference variable, while the other compositional variables remain constant (Valle et al., 2024). These constraints do not apply to the number of trees, which acts as an absolute independent predictor variable.

For classification of the flux density measurement points and transects, a different approach was taken. The flux densities along the defined transect of a street canyon within the urban canopy layer can be expected to possess the footprint of that same street canyon. Therefore, the transects were directly defined individually, oriented at the classification in Žgela et al., 2024 (Figure 2.10). The static measurement surroundings were classified accordingly for intercomparison.

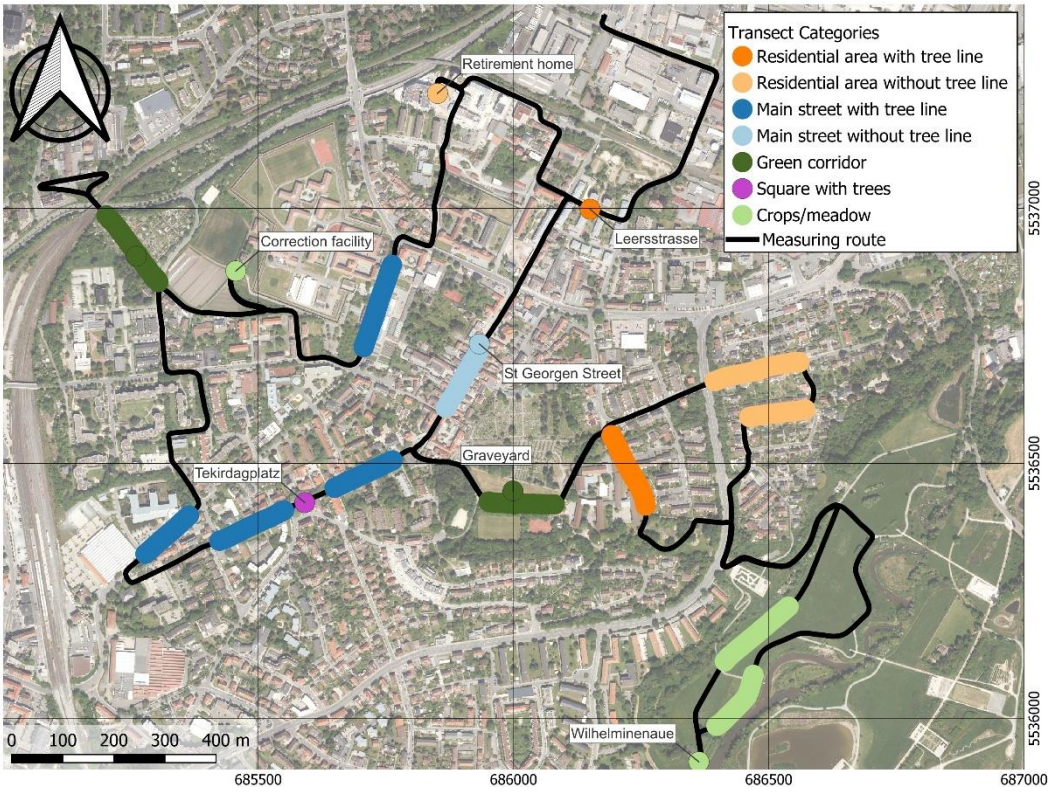

Figure 2.10: Map of the approximately homogeneous street transects used for the perturbation times of the atmospheric flux measurements. Map by Sophie Resch. Map material was provided by the State Institute for Geodesy of Bavaria (Bayerische Vermessungsverwaltung, 2025).

2.3.6 Quality assurance

To check the quality of the MWS that were used to extend the MiSKOR network, the stations were tested next to each other at the EBG station. Bias (b), comparability (c) and precision (p) of the measured parameters were calculated using equations 2.12a-c. The EBG was used as reference. The results are shown in Figure 2.11.

$$b = \frac{1}{N}\sum_{i=1}^{N}(x_{1i} - x_{2i}) \quad 2.12a$$

$$c = \left[\frac{1}{N}\sum_{i=1}^{N}(x_{1i} - x_{2i})^2\right]^{0.5} \quad 2.12b$$

$$p = \sqrt{c^2 - b^2} \quad 2.12c$$

b = bias, c = comparability, p = precision 1 = compared station, 2 = etalon

The T_{air} measurement quality was considered sufficient. For the relative humidity, no correction formula was found to adjust for the bias of the GY station. It was left out for further humidity evaluations. The GY station also showed a bias for the solar radiation. A correction factor was calculated as the quotient of the mean solar radiation across all

stations and the mean solar radiation at the GY site over the entire test period. This correction factor was multiplied with the whole GY solar radiation dataset.

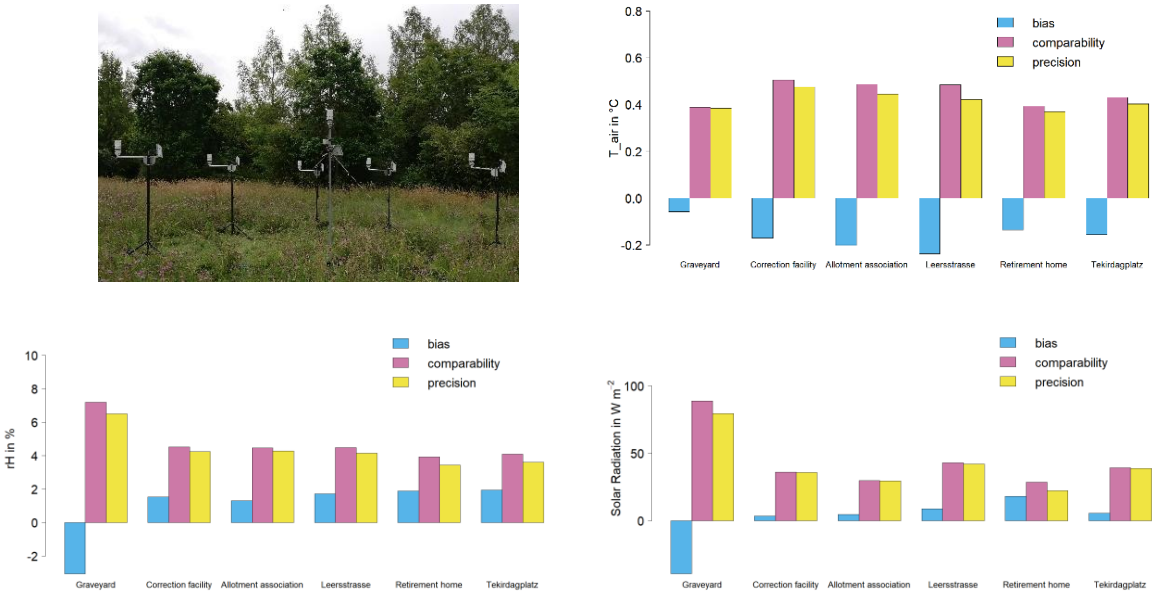

Figure 2.11: Setup of the comparison measurement in the EBG (top left). Results include comparisons of T_{air} in °C (top right), relative humidity (rH) in % (bottom left) and Solar radiation in W m^{-2}.

Mean temperature and humidity values were compared between MobiFast and the MWS for the 2 minute stops. In this case, the MobiFast values were used as reference. The temperature bias at the WA MWS exceeded the biases at the other MWS by roughly 1 °C. The station was excluded from the evaluation of T_{air} and the EBG station was chosen as replacement rural reference. The biases of the WA and SG *e* values were 4-5 times as high as for the other MWS. Since three of the originally eight MWS showed a distinct bias in the humidity values, the evaluation of humidity perturbations was limited to the results of the measurement rides. Lastly, the Tekridagplatz station was excluded from any evaluation as it was only setup at the beginning of August.

Parts of the ride data were missing due to problems with the logging of anemometer and gas analyzer data. Only the measurement ride during the 14th of August was completely recorded successfully. The measurement ride during the 12th of August is missing the last section between the SG and the LS MWS. The measurement ride during the 30th of July was originally a test ride. It was not begun at BayCEER but at the TP, passing the SG MWS before following the original route starting at the LS MWS. This measurement ride is even missing the whole section after the WA MWS. Because of the limited data yield and to reduce stochastic effects as described earlier, it was decided to average the perturbations of the three rides together. This way, every part of the route is at least represented twice.

For the eddy covariance measurements, the following checklist was compiled to assure data quality:

- Review co spectra to determine perturbation time scale
- Calculate motion corrected fluxes and turbulence statistics using bmmflux
- Steady state conditions are assumed to be fulfilled for short perturbation time scales and along homogeneous street transects
- Filter spectral frequency correction factor > 1.5 that were calculated for the correction after Moore (Moore, 1986)
- Filter mean vertical wind > 0.2 (Foken, 2017)
- filter beta rotation > 15° (Figure 2.12)

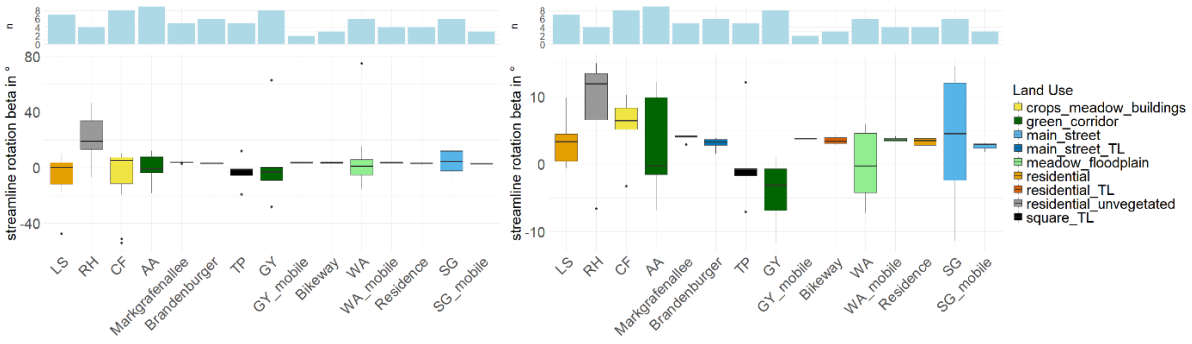

Figure 2.12: Distribution of the beta rotation value throughout the St Georgen/ Burg neighboruhood for the three measurement rides before (left) and after (right) filter application. The beta rotation value resembles the rotation angle of the second coordinate rotation of the EC double rotation.

3 Results and preliminary discussion

In the following chapter, the results of the data evaluation are shown in four subchapters concerning the continuous stationary MWS measurements (chapter 3.1), the MobiFast measurements of T_{air} and e perturbations (chapter 3.2), the MobiFast measurements of turbulent energy fluxes (3.3), and supplementary measurements (chapter 3.4). To avoid redundancy and divergence in the result descriptions of observed phenomena and their contextualisation, preliminary discussions are conducted for the presented results. At first, an overview is given of the synoptic weather conditions during the measurement period according to the criteria defined in 2.3 (Figure 3.1). 9 autochthonous days were identified which were used for further data evaluation.

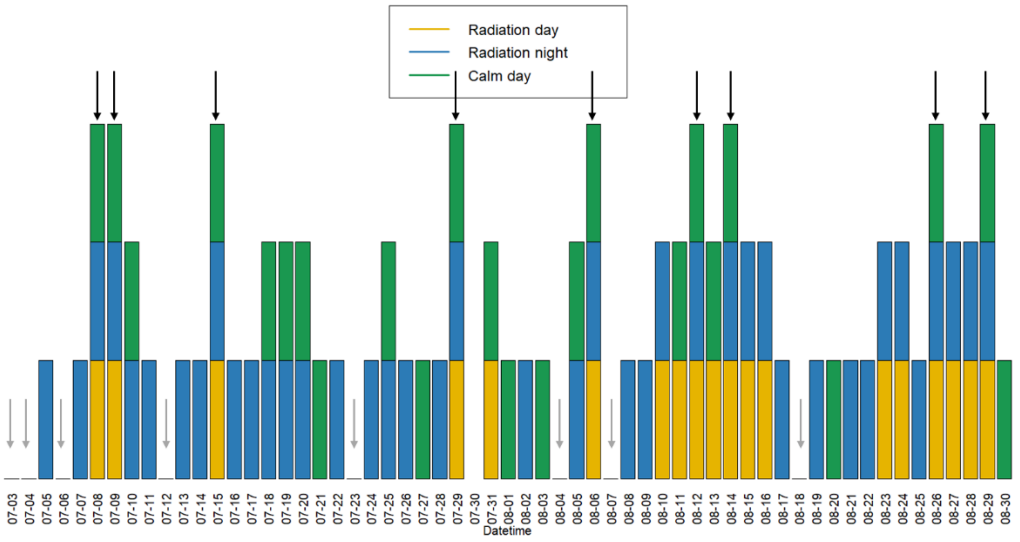

Figure 3.1: Overview of synoptic conditions during the entire measurement period. The radiation day, radiation night and calm day selection criteria are defined in chapter 2.3. Days marked with a black arrow were classified as autochthonous, days marked with a grey arrow were classified as allochthonous. The measurement rides considered for this thesis were conducted on the 30th of July and the 12th and 14th of August in the afternoon.

The 30th of July was not classified due to missing solar radiation data in the EBG. In the previously used classification using the WA MWS, the day was also classified as autochthonous. The day was not used for the data evaluation of the MWS data. Since one of only three successful measurement rides was conducted that day, and it was also identified as a potential autochthonous day in advance to the ride, the ride data was still used for the MobiFast data evaluation.

3.1 Spatial perturbation of air temperature and humidity during autochthonous conditions – from noon to midnight

With the MWS network, differences in the diurnal course of T_{air} during autochthonous conditions could be detected between the different measurement locations. The absolute temperature progression can be seen in Figure 3.2. The mean T_{air} was highest

at the SG MWS for the whole day except for the early morning. A maximum temperature plateau is seen approximately between 16:00 and 18:00 for all MWS. The autochthonous days show a net temperature increase within the 24 h time period for all locations. This increase is mostly found for autochthonous days following mixed synoptic days according to the classification defined in 2.3. An autochthonous day following a day of mixed synoptic conditions was therefore associated with a net temperature increase in the mean diurnal temperature course. No general statements about consecutive succession of autochthonous days are possible, since only one pair occurred during the measurement period (Figure 3.1).

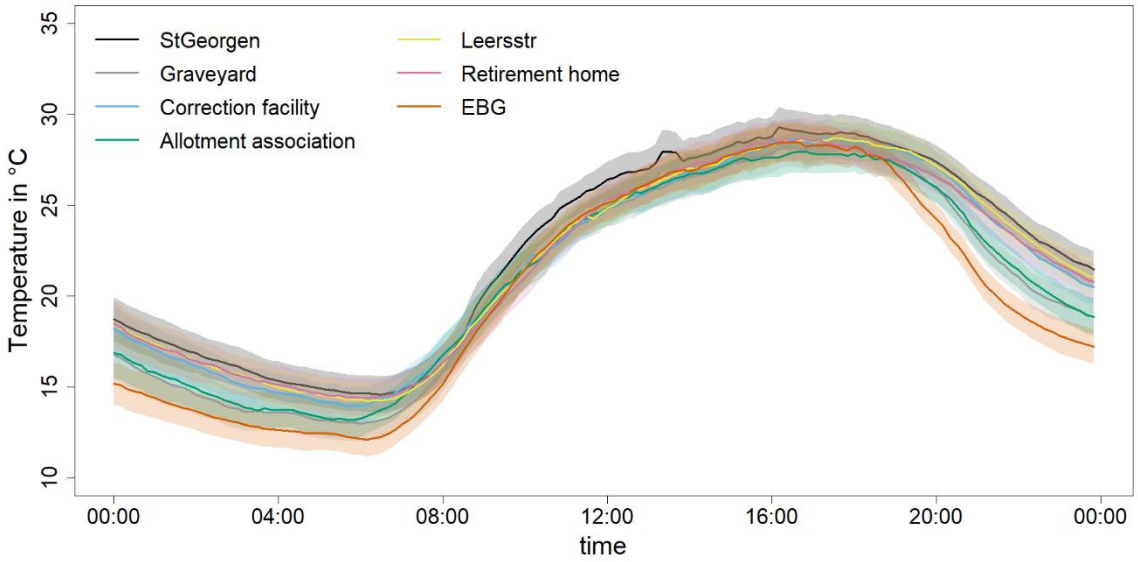

Figure 3.2: Mean diurnal course of T_{air} (Temperature) during autochthonous days (9) in July and August at the eight MWS. Standard errors are shown behind the mean as semi-transparent polygons of the same colour. The allochthonous comparison plot is found in the appendix (Figure 8.5)

A more detailed look at T_{air} differences between the stations can be achieved by subtracting the EBG rural reference value from all MWS values (Figure 3.3). Here, four time phases can be identified between noon and midnight. Around noon, mean T_{air} at the SG MWS is around 1.5 K higher than at the EBG station. The SG MWS is located in a densely closed street canyon with a low albedo cobblestone road. During noon it is exposed to direct solar radiation while longwave radiation is partly trapped by the surrounding street canyon. The other MWS T_{air} values are closer together in that time frame with the EBG and RH being slightly higher. During the afternoon the MWS T_{air} values stay within a +/- 1 °C boundary relative to the EBG values. The SG MWS is still the warmest while the AA shows the coolest T_{air}. The AA and GY stations are surrounded by trees and partly short vegetation, providing evapotranspirative cooling. The AA location is partially shaded due to a treeline. Throughout the late afternoon the differences to the EBG increase drastically, resulting in three distinct groups: The EBG T_{air} is by far the lowest, followed by the AA and GY temperature, at around 2 °C higher. Temperature differences of 4-5 °C relative to the EBG can be seen for the other MWS value. At the beginning of the night, the T_{air} differences between the EBG and the other MWS start decreasing slowly.

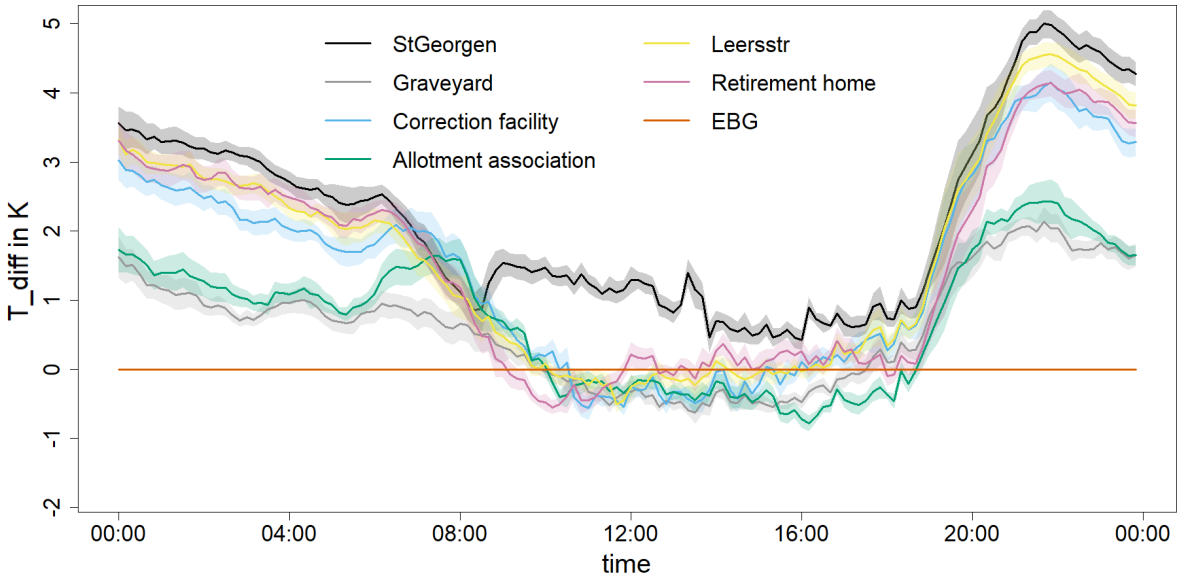

Figure 3.3: Mean diurnal course of differences in T_{air} (Temperature difference) between the six measurement locations and the EBG reference for the nine autochthonous days during the measurement period. Standard errors are shown behind the mean as semi-transparent polygons of the same colour. The allochthonous comparison plot is found in the appendix (Figure 8.6)

To take a closer look at the three more stable phases of this temperature progression in context of the surrounding land use, boxplots of 60 min mean T_{air} differences were created for solar noon, the afternoon heat peak and the last hour of the day (Figure 3.4). During noon, highest T_{air} are associated with the highest share of building and pavement area at the SG MWS with T_{air} being around 1 K higher than at the EBG. T_{air} for the less densely built MWS of LS and RH were similar to the EBG value. Distinctly lower T_{air} differences of around -0.5 K are found for the MWS with the lowest share of building area and in case of the AA and GY, an amount of around ¼ of high vegetation share including the "gardens" land use category. In the afternoon heat peak, the T_{air} distribution of the three most densely built stations still follow the trend of lower temperatures around lower building area shares. The AA and GY values are still the lowest, with the T_{air} at the GY being distinctly warmer even though the GY has lower surrounding building area share. T_{air} at the CF now tends to being increased, deviating from the pattern of lower building area share being associated with lower temperatures. At night T_{air} is increased with an increasing share of building areas and can be categorized into the three previously described groups. The CF T_{air} is closer to the more densely built location T_{air} values than to the GY and AA T_{air} values, even though its land use surroundings closer resemble those of the GY and AA.

The most instationary phase seen in Figure 3.3 is characterized by a rapid decrease in T_{air} (Figure 3.2) due to a rapid decrease in solar radiation as the main heating source (Figure 3.16). It was investigated by creating linear models showing the mean temperature decrease within the hour of the highest T_{air}-reduction at the EBG (Figure 3.5). Here the slopes represent the mean cooling rate resembling the three groups identified for night-time in Figure 3.3. The cooling rate at the CF is the greatest of the warmest four stations

and the GY cooling rate is greater than the AA one. In both cases the cooling rate is greatest for the MWS with the lowest share of building and pavement area within their group. The cooling rate at the EBG is by far the greatest at around 5 K h^{-1}.

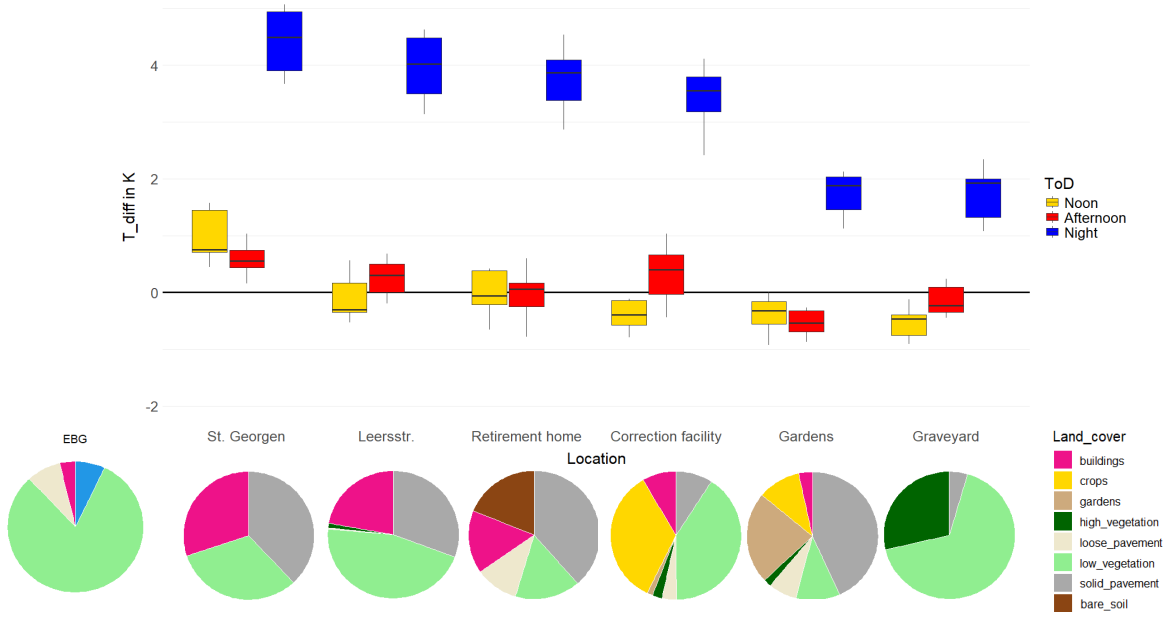

Figure 3.4: Hourly mean of differences in T_{air} (T_diff)between the six measurement locations and the EBG reference for three times of the day visualized in a boxplot (above). Noon hour was classified as +/- 30 minutes around solar zenith, afternoon hour was classified as 60 minutes of highest mean T_{air} in the EBG, and night hour was classified as the last hour of the day (23:00-00:00). Additionally, the respective land use distribution is shown for the six measurement locations (below). The allochthonous comparison plot is found in the appendix (Figure 8.7)

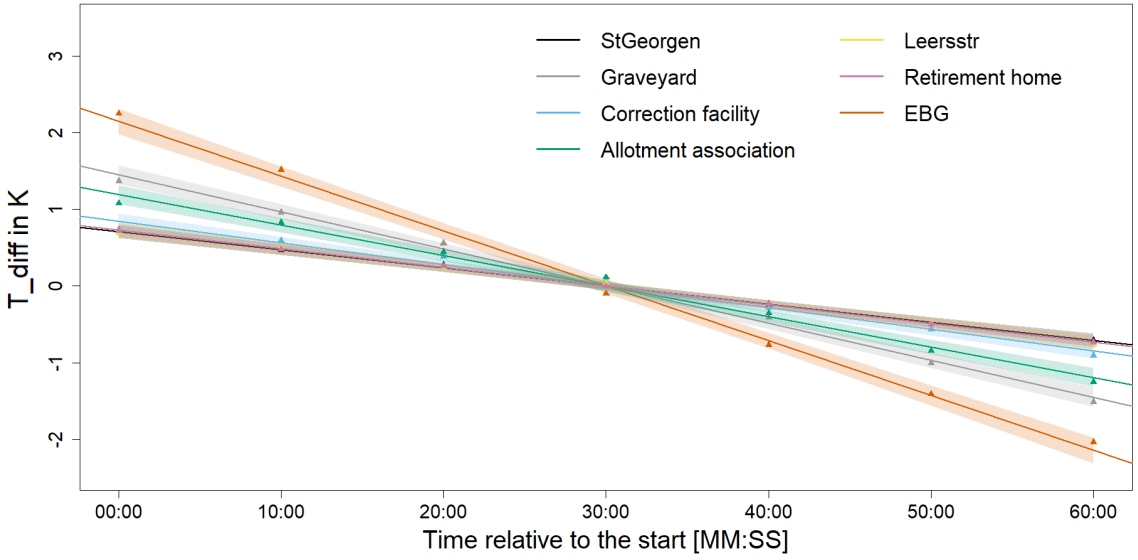

Figure 3.5: Mean relative T_{air} development (T_diff) for the six measurement locations and the EBG reference during the late afternoon transition (LAT) of the nine autochthonous days with linear models. For the LAT time frame selection, the hour of maximum temperature reduction measured in the EBG was used. The mean temperature of the whole hour was then subtracted for each individual day and station. Linear models were fitted using the single 10-minute averages of all days combined. Here, only the mean of the 10-minute averages for each timeslot is plotted. The allochthonous comparison plot is found in the appendix (Figure 8.8)

The results can be explained using the energy budget equation (equation 1.1) in context of the surrounding land use. Sealed surfaces with reduced albedo and surrounding heat storing building mass can enhance surface heating, if direct radiation isn't blocked by

surrounding buildings. With the increased radiation budget, stored heat in the surrounding buildings, missing advection during autochthonous conditions and a lack of water availability for the latent heat flux due to surface sealing, the upward sensible heat flux is enhanced, heating the air mass within the urban canopy layer. This is seen at the SG MWS where the street canyon is exposed to direct solar radiation during noon, causing a T_{air} increase of approximately 1 K relative to the EBG, but partially shaded during the afternoon, causing a T_{air} difference of approximately 0.5 K relative to the EBG. High vegetation areas can reduce the radiation budget through shading and enhance the latent heat flux by retaining water for evapotranspiration, resulting in a decreased heating of the ground surface and therefore a decreased upward sensible heat flux. The hereby reduced heating of the canopy layer air mass results in the reduced T_{air} observed at the AA and GY during noon and afternoon. Deviations from the pattern of higher T_{air} at locations of high surface sealing and building area share can be attributed to a reduced cumulative radiation budget caused by building induced shading. Surrounding buildings that partially re-absorb outgoing longwave radiation from the ground surface and partially emit stored heat back into the urban canopy layer can reduce cooling rates during the late afternoon resulting in strong T_{air}-differences during early night.

3.2 Spatial perturbation of air temperature and humidity during autochthonous conditions – the afternoon heat peak

For the three measurement rides, detailed maps of high-resolution mean T_{air} and e perturbations within the urban canopy layer could be created. The mean T_{air} perturbation map shows patterns with T_{air}-differences of up to 3 K (Figure 3.6). Temperature peaks can be seen at the Markgrafenallee, east to the CF. They might be associated to close traffic at the turns as an anthropogenic heat source. T_{air} values elevated by approximately 1 K are present at the industrial area in the northeast, the Markgrafenalle, at the street south of the CF MWS, at the main street between GY and WA, and in the residential area in the east, north of the WA. T_{air} elevated by around 0.5 K are seen at SG, the LS, east of the GY and in the residential area between TP and AA. All elevated temperatures were associated with pavement and buildings within their immediate surroundings. As these provide no water retention, heat cannot be transported away from the surface through the latent heat flux resulting in heat accumulation and strong upward sensible heat fluxes, heating the air within the urban canopy layer. The lowest temperatures are found in areas of high vegetation aggregation like the WA, the GY bikeway, the AA and the bikeway between WA and GY. T_{air} northeast of the RH is reduced as well. T_{air} at the Brandenburger street adjacent to the TP is close to the calculated MWS mean and reduced compared to other main streets like the Markgrafenallee and SG. The Brandenburger street is the main street with the densest treeline that was part of the measurement route, reducing the available radiation budget. Except for reduced temperatures due to shading by high buildings, like it was observed northeast to the RH MWS, reduced T_{air} can be attributed to surrounding

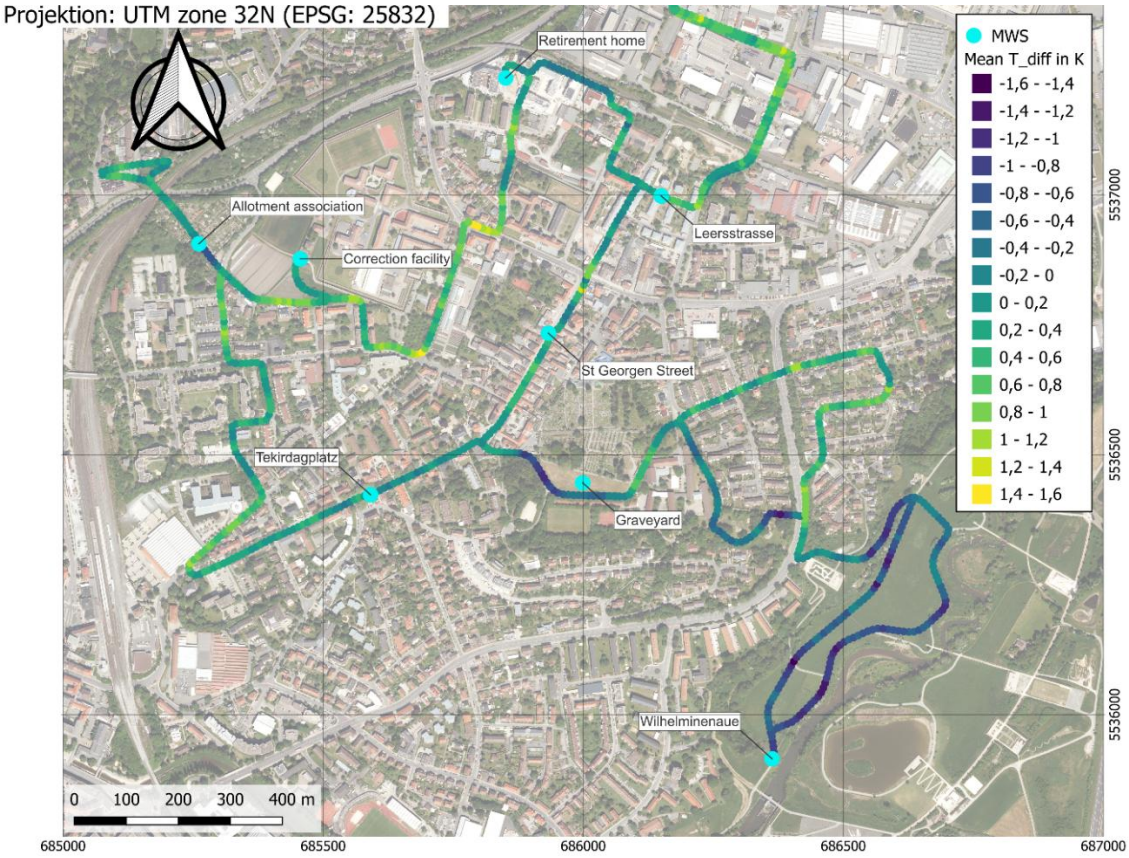

Figure 3.6: Mean spatial perturbation of T_{air} relative to the MWS network (T_diff) during the three measurement rides on the 30th of July and the 12th and 14th of August in the afternoon. Map material was provided by the State Institute for Geodesy of Bavaria (Bayerische Vermessungsverwaltung, 2025).

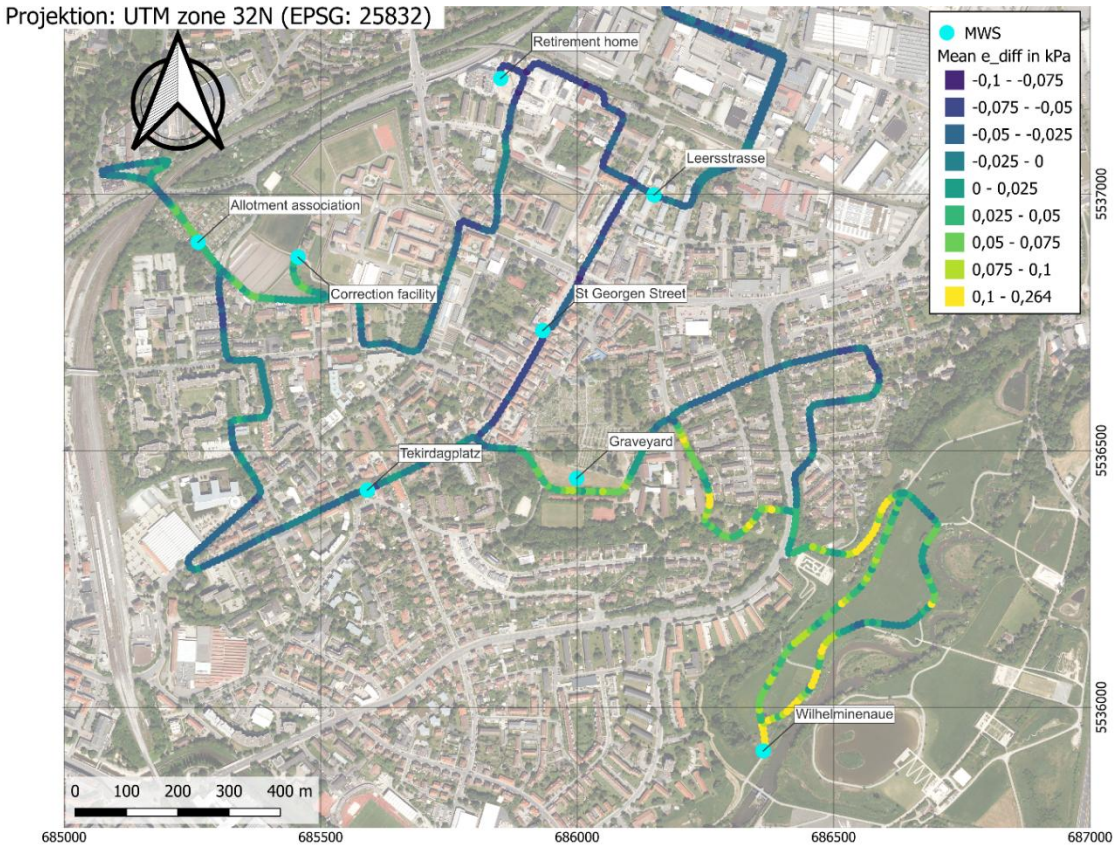

Figure 3.7: Mean spatial perturbation of e relative to the MWS network (e_diff) during the three measurement rides on the 30th of July and the 12th and 14th of August in the afternoon. Map material was provided by the State Institute for Geodesy of Bavaria (Bayerische Vermessungsverwaltung, 2025).

vegetation. Contrary to building and pavement areas, vegetation areas can retain and provide water for the latent heat flux, resulting in accumulation of water in the canopy layer air instead of sensible heat. They additionally provide shade in case of high vegetation, reducing the locally available radiation budget.

The water accumulation at vegetated areas or a lack thereof around pavement and building areas is observed for the e perturbation (Figure 3.7). Throughout most of the lower urban canopy layer along the route, e is reduced with the lowest values found along the St Georgen street and northeast of the RH. e is increased around the GY, the WA and the bikeway in-between, as well as around the AA and the CF.

To investigate the correlation between land use properties and the perturbations of T_{air} and e, compositional linear models were fitted to the spatially averaged measurement ride data (Figure 3.8, Figure 3.9). To assess the applicability of the models for urban-rural and urban-urban comparisons, the models were created for the whole dataset as well as for a subset missing the whole data from the WA floodplain meadow and the industrial area north of the St Georgen/ Burg district. The subset area will from here on be referred to as “district area”. The model parameters are shown in Table 3.1. To avoid multicollinearity, the building area share was left out as the reference variable as explained in chapter 2.3. For the whole dataset, the T_{air} showed moderate decrease for an increased number of trees and an increased share of pavement area, coinciding with a reduction of building area (Figure 3.8). Stronger temperature decreases can be seen for increasing area shares of low vegetation, high vegetation and water relative to building area. It should be noted that for low amounts of low vegetation and pavement, the temperature is still at around + 0.5 K above the subtracted MWS mean. The model has an R^2 value of approximately 0.44, meaning that close to half of the T_{air} perturbation can be explained by the model (Table 3.1). When applying the model just to the district area data, the R^2 value drastically shrinks to around 23.5 %, showing a drastic decrease in the explanatory power of the model. Significant decreases in T_{air} are now only associated with increasing number of trees and increasing area share of high vegetation. This leads to the interpretation that the moderate inverse correlation between pavement and T_{air} as well as low vegetation and T_{air} were mainly caused by the reduced temperatures in the WA floodplain meadow. The linear regression model for the whole e data in dependence of the land use shows effects, opposite to those of the whole $\mathrm{T_{air}}$ data model (Figure 3.9). Its explanatory power is greater, with an R^2 value of around 0.65. When applying the model only to the district area data, the effects stay similar, and the R^2 value is only reduced by approximately 0.025 (Table 3.1).

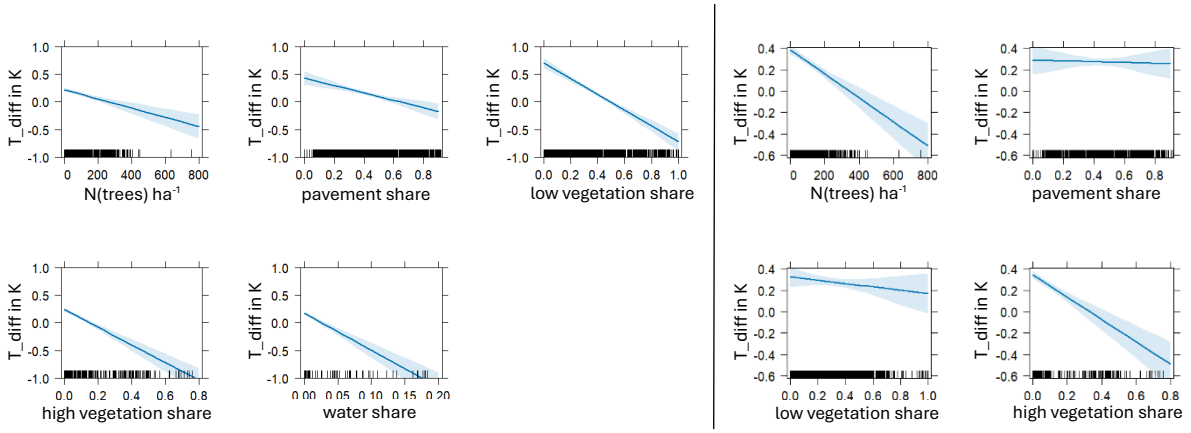

Figure 3.8: Visualisation of a compositional linear model between land use and relative T_{air} (mean_Tdiff). The model shown in the five plots on the left include the WA river floodplain meadow and the industrial area, the model shown in the four plots on the right doesn't. Since there is no open water along the measurement route outside the WA, the variable is missing in the right model. The sum of the land use values (except for the number of trees, as it is additionally calculated as trees per ha) amounts to 1 together with the area of buildings. By leaving the building area out, the effect due to an increase of one land use area can be interpreted as replacing building area with that respective land use area. The vertical lines at the bottom of the plot visualize data density.

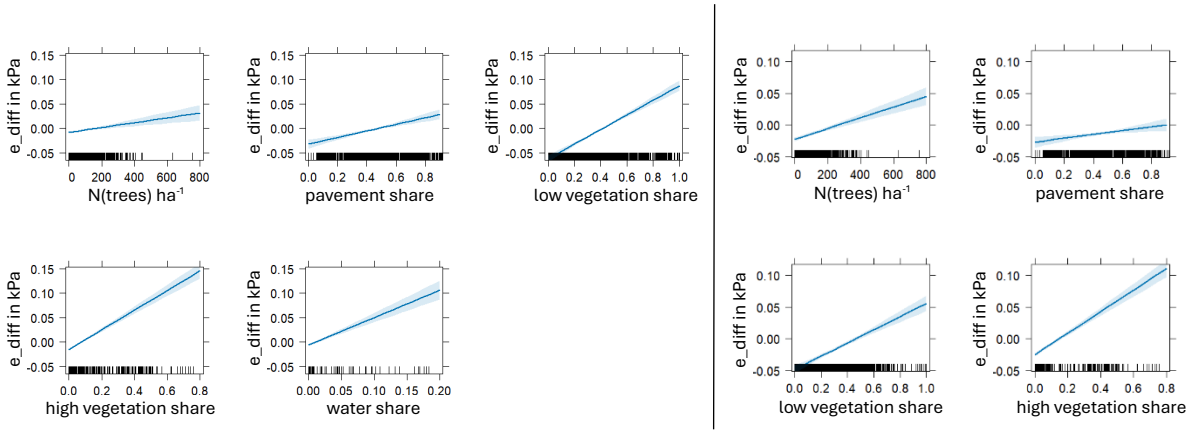

Figure 3.9: Visualisation of a compositional linear model between land use and relative e (mean_eDiff). The model shown in the five plots on the left include the WA river floodplain meadow and the industrial area, the model shown in the four plots on the right doesn't. Since there is no open water along the measurement route outside the WA, the variable is missing in the right model. The sum of the land use values (except of the number of trees) amounts to 1 together with the area of buildings. By leaving the building area out, the effect due to an increase of one land use area can be interpreted as replacing building area with that respective land use area. The vertical lines at the bottom of the plot visualize data density.

Table 3.1: Table of the model characteristics of the multifactorial linear models of land use vs relative T_{air} and e perturbations. The detailed factors can be seen in the appendix at page 58.

Land use vs.	T_{air}	T_{air}	e	e
Wilhelminenaue (WA)	Included	Not included	Included	Not included
Figure	Figure 3.8	Figure 3.8	Figure 3.9	Figure 3.9
N (Significant factors)	5/5	2/4	5/5	4/4
R^2	0.4431	0.2354	0.6468	0.6205

To take a closer look into the relation between T_{air} and e, two more linear regression models were fitted for the whole measurement ride data and the district subset area data (Figure 3.10). The models resembled the findings of the land use distribution models by showing a strong correlation between T_{air} and e when including urban and rural environments, that is weakend when only looking at the inner district variabilities. Lastly,

T_{air} was evaluated in relation to the sum of low and high vegetation within the St. Georgen/ Burg district (Figure 3.11). A significantly lowered mean T_{air} was only present for the highest 10 percent quantile of vegetation cover, while the occurrence of T_{air} minima below -0.5 K already began at the median quantile.

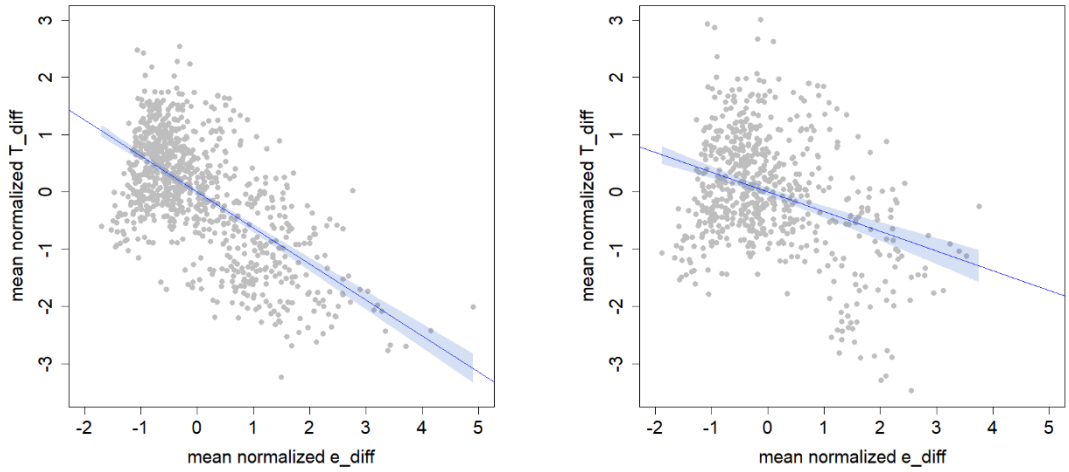

Figure 3.10: Relation between normalized T_{air} and normalized e, visualized by linear models for the whole ride data (left) and the data subset missing the WA floodplain meadow and the industrial area (right). The R^2 values were roughly 39% and 12 % respectively. Both models were significant.

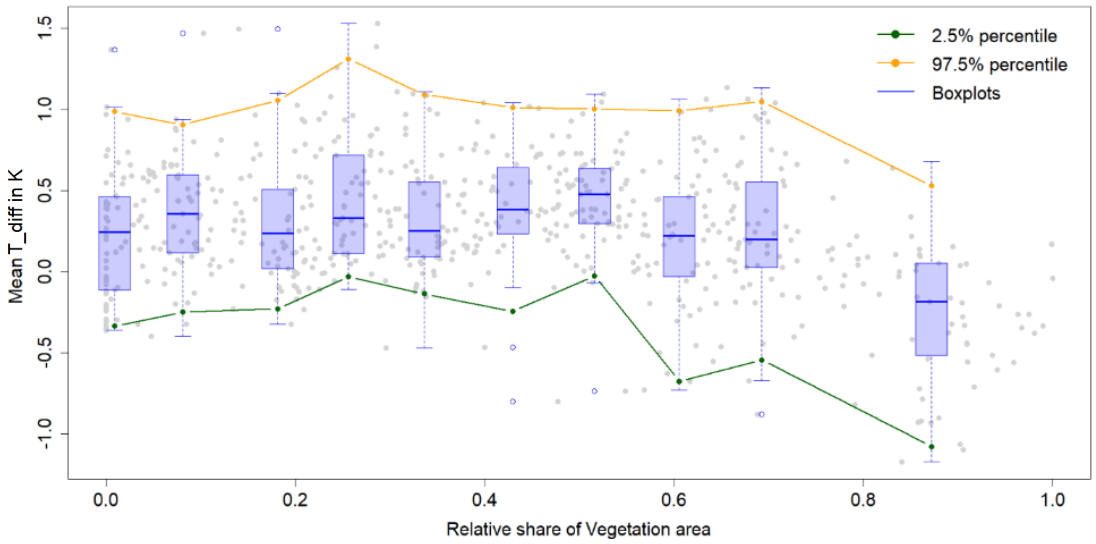

Figure 3.11: Spatial mean of T_{air} perturbation (Mean T_diff) during the three measurement rides without the WA versus the share of vegetation area. The 10 bins for the boxplots were applied for equal quantiles. A heatmap of the significance values can be found in the appendix in Figure 8.10.

3.3 Spatial distribution of turbulent energy fluxes during the afternoon heat peak

For the previously defined transects, TKE and turbulent energy fluxes could be calculated for the afternoon heat peak measurement rides. As described in chapter 2.3, only the high frequency part of the spectrum is observed in this study. Therefore, the focus is set on comparing differences in TKE and energy flux magnitude. The TKE shows distinct

differences, especially between stationary and mobile measurements (Figure 3.12). The mobile measurements show a tendency towards increased TKE relative to the measurements done statically next to the eight MWS. This bias is further discussed in chapter 4.3. For the stationary measurements, the TKE was highest at the CF and SG and lowest at the WA, LS and the AA. The mobile measurements showed highest TKE at the SG and WA transect and lowest TKE at the GY bikeway. The LS, AA and GY bikeway are surrounded by wind-shielding vegetation or buildings preventing larger eddies from reaching the ground surface and contributing to the TKE budget. In contrast, the SG location is characterized by a wide corridor, and the CF is exposed to the north allowing for larger eddies to reach close to the ground surface. Both the mobile and static WA locations are exposed, but with the adjacent trees in the west and river in the east, the mobile transects are closer to roughness elements, possibly enhancing turbulent fluctuations.

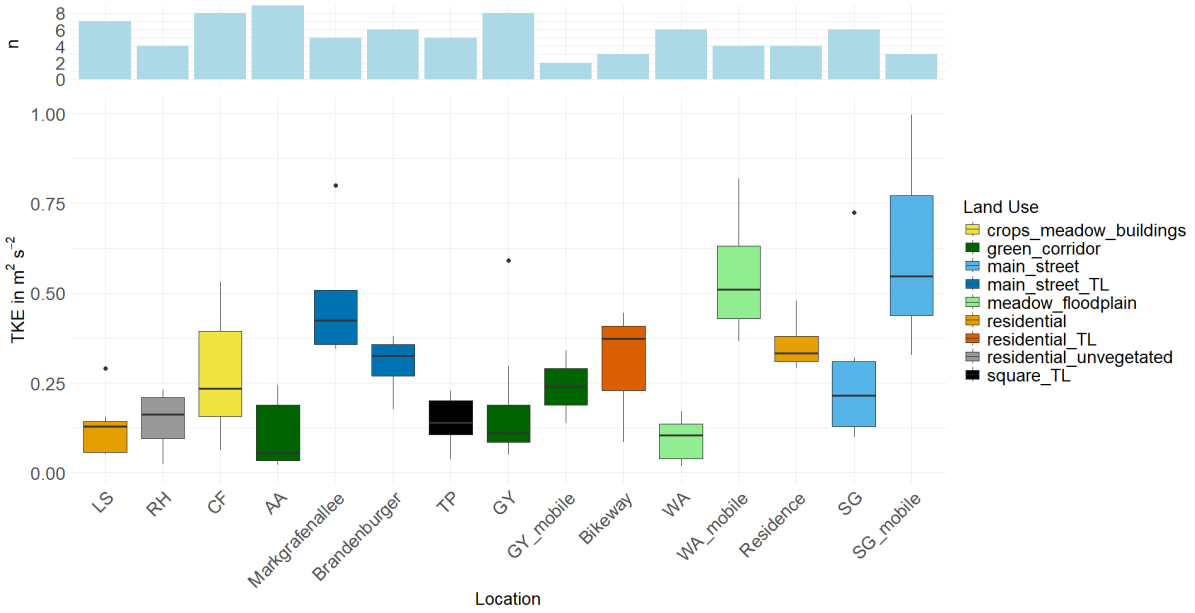

Figure 3.12: Distribution of turbulent kinetic energy (TKE) within the St Georgen/ Burg neighbourhood during the three measurement rides on the 30th of July and the 12th and 14th of August in the afternoon. Similar land use types are marked in the same colour. The "TL" suffix indicates that a land use type possessed a treeline. The number of single data points is visualized in the upper graph. The two letter abbreviations along the x-axis stand for measurements conducted during the 2-minute stops at the MWS. If a "mobile" is added the measurements were taken during the ride at the immediate surrounding around the MWS. The Abbreviations stand for: LS = Leersstrasse, RH = Retirement home, CF = Correction facility, AA = Allotment association, TP = Tekirdagplatz, GY = Graveyard, WA = Wilhelminenaue, SG = St Georgen street.

In the following, the sensible and latent heat flux distributions shown in Figure 3.13 and Figure 3.14 respectively, will be described for the different locations in respect to the approximate energy budget and available water. The lowest and partially even negative sensible heat fluxes are found at the AA, GY and the bikeway between GY and WA (Figure 3.13). The RH and SG MWS locations are also showing reduced sensible heat fluxes while the SG-mobile sensible heat flux is distinctly higher (Figure 3.13, Figure 3.16.). Elevated sensible heat fluxes can also be seen for the CF, LS, Markgrafenallee and Residence (Figure 3.13). Lastly, the WA only shows a moderate sensible heat flux but an increased

latent heat flux (Figure 3.13, Figure 3.14). Except for the CF, WA, AA, TP and GY, all locations show a distinctly reduced latent heat flux (Figure 3.14)

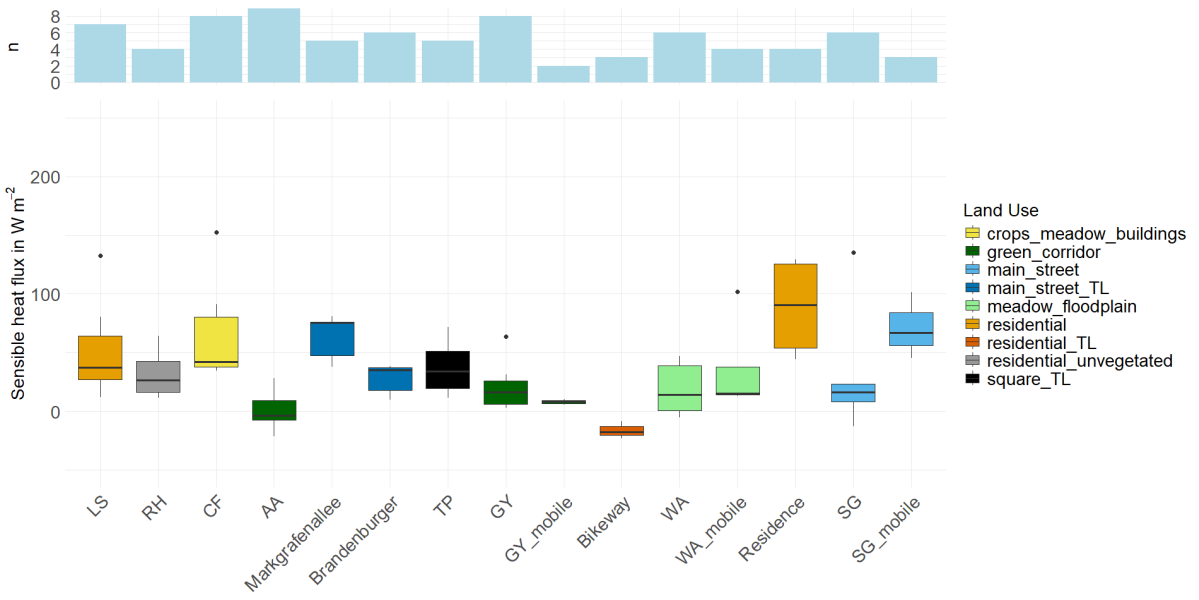

Figure 3.13: Distribution of sensible heat fluxes within the St Georgen/ Burg neighbourhood during the three measurement rides on the 30th of July and the 12th and 14th of August in the afternoon. Similar land use types are marked in the same colour. The "TL" suffix indicates that a land use type possessed a treeline. The number of single data points is visualized in the upper graph. The two letter abbreviations along the x-axis stand for measurements conducted during the 2-minute stops at the MWS. If a "mobile" is added the measurements were taken during the ride at the immediate surrounding around the MWS. The Abbreviations stand for: LS = Leersstrasse, RH = Retirement home, CF = Correction facility, AA = Allotment association, TP = Tekirdagplatz, GY = Graveyard, WA = Wilhelminenaue, SG = St Georgen street.

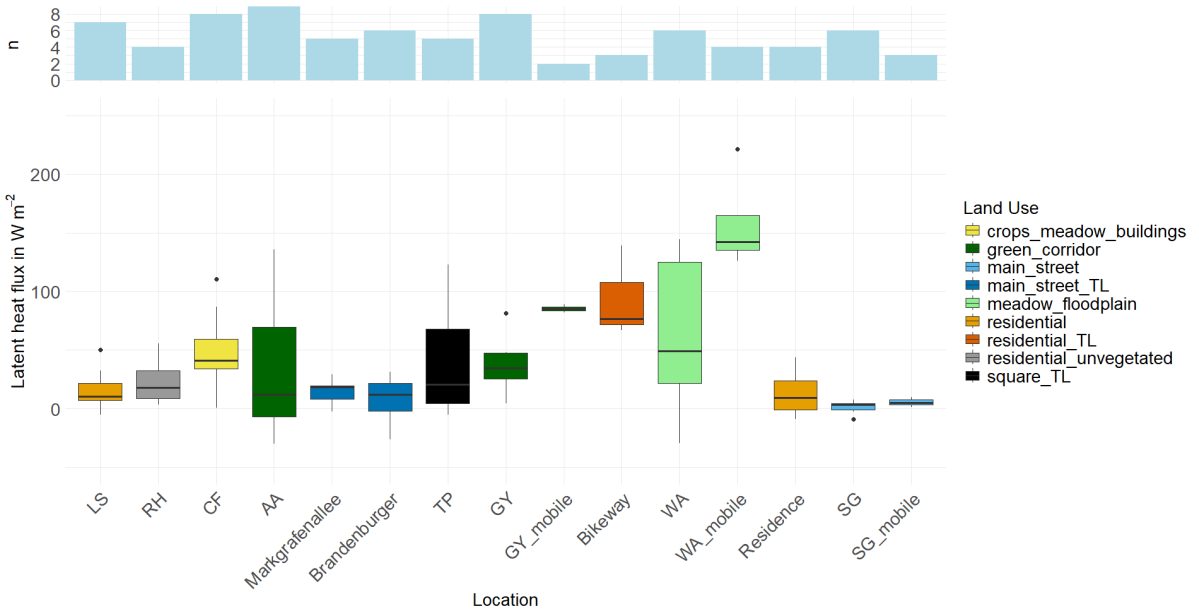

Figure 3.14: Distribution of latent heat fluxes within the St Georgen/ Burg neighbourhood during the three measurement rides on the 30th of July and the 12th and 14th of August in the afternoon. One outlier in the WA location of around 400 W m^{-2} is not included in the graph to not disturb comparability of the boxplots. Similar land use types are marked in the same colour. The "TL" suffix indicates that a land use type possessed a treeline. The number of single data points is visualized in the upper graph. The two letter abbreviations along the x-axis stand for measurements conducted during the 2-minute stops at the MWS. If a "mobile" is added the measurements were taken during the ride at the immediate surrounding around the MWS. The Abbreviations stand for: LS = Leersstrasse, RH = Retirement home, CF = Correction facility, AA = Allotment association, TP = Tekirdagplatz, GY = Graveyard, WA = Wilhelminenaue, SG = St Georgen street.

The three locations AA, GY and bikeway between GY and WA are covered by a treeline, reducing the radiation budget available for turbulence inducing surface warming. This can be explained by shading and efficient energy dissipation above the treeline due to evapotranspiration, leading to reduced temperature and thereby reduced longwave downward radiation from the leaf ceiling. Additionally, the locations are less water limited than the district parts with sealed surfaces, allowing for a part of the available energy at the surface to be transported away via the latent heat flux (Figure 3.7). This also explains the reduced T_{air} at these locations as the radiation reaching and heating the surface is reduced, the upward heat flux from the surface transports heat partly via the latent heat flux not causing increased T_{air} , and the downward sensible heat flux from the leaves is reduced due to a strong upward latent heat flux caused by evapotranspiration. Both the RH and SG MWS locations are shaded during the afternoon, reducing the available energy due to direct solar radiation for the surrounding surfaces and causing lower sensible heat fluxes despite their severe water limitation (Figure 3.7), that prevents latent heat fluxes to transport energy away from the surface without heating of the urban canopy layer air. The SG-mobile measurement of the sensible heat flux took place on the easterly side of the road, that was not shaded during the afternoon measurement rides. The surface heating is intensified here by the low albedo due to the dark cobblestone, causing increased energy availability at the ground surface due to decreased reflection of solar radiation. This increased energy availability along with the high TKE explain the elevated temperatures, created by a strong heat transfer from the ground into the urban canopy layer air layer via the sensible heat flux. The LS, Markgrafenallee and Residence are widely exposed to solar radiation during the afternoon and mainly characterized by soil sealing due to pavement and surrounding buildings (Figure 2.4). This explains the increased sensible heat flux due to a respectively increased energy budget and reduced water availability for the sensible heat flux. The increase of the upward sensible heat flux along the three main streets from Brandenburger street to Markgrafenallee and then to the SG-mobile location coincide with a decreasing density of the treeline and therefore an increase in the availability of energy at the ground surface due to solar radiation. The treeline is very dense above the Brandenburger street, reduced above the Markgrafenallee and absent at SG. The CF is even more exposed than the previously described stations, but part of the available energy is transported away from the surface via the latent heat flux, which is enabled by the adjacent unsealed crop field and is not causing any T_{air} increase (Figure 3.14).

The WA exposition to the open sky is similar to the CF exposition but shows a sensible heat flux more similar to the RH and SG MWS location (Figure 3.13). Here, most of the available energy is transported away from the surface via the latent heat flux as the surrounding floodplain valley provides sufficient amounts of water (Figure 3.14). The same is also applicable for the bikeway, the AA and the GY (Figure 3.15). The reduced water availability at all measurement locations except for the CF, WA, AA, TP and GY, explains the dominating sensible heat flux at these locations visualized in Figure 3.15.

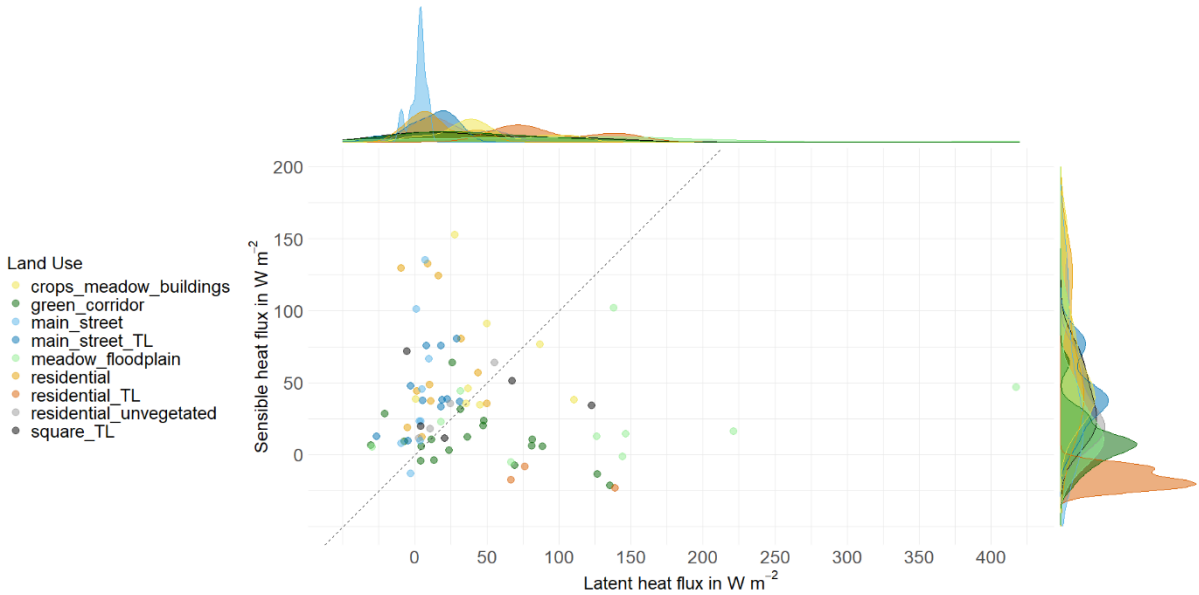

Figure 3.15: Visualisation of the bowen ratio as data distribution in a plot of latent vs sensible heat fluxes for the three measurement rides. All values in the top left corner possess a bowen ratio >1, all values in the bottom right corner posess a bowen ratio <1. Points along the angle bisector represent a bowen ratio of 1.

3.4 Supporting measurements of solar radiation and wind

Supplementary to the measurements of T_{air}, e, and turbulent energy fluxes, solar radiation was measured at the seven MWSs. The solar radiation is the main source of energy for the surface energy budget and therefore the heating of the urban canopy layer through turbulent energy fluxes. Its diurnal course is mainly impacted by the surrounding land use for autochthonous conditions. Identifying time periods of reduced solar radiation can explain immediate effects of reduced energy availability like reduced turbulent energy flux densities, while assessing the cumulative energy budget over the course of the day can explain T_{air} patterns. During autochthonous synoptic conditions, the diurnal course of solar radiation showed some distinct differences between the measurement locations (Figure 3.16). All MWS except for the AA and the CF experience a shading induced delayed increase of solar radiation in the morning. All MWS, except for the GY station, show a sharp dip in solar radiation due to shading by the lamp post they are installed to during the day. The SG, AA and RH MWS experience the drastic reduction of solar radiation in the afternoon earlier than the other MWS. This effect is caused by shading of higher buildings in case of SG and the RH or the tree canopy in case of the AA. The already decreased solar radiation during the afternoon at SG, RH and AA can explain the reduced turbulent flux densities observed during the afternoon measurement rides (Figure 3.13, Figure 3.14). In case of the RH, the overall reduced solar radiation budget over the diurnal course can explain the reduced T_{air} for a location with such low water availability for evapotranspirative heating reduction.

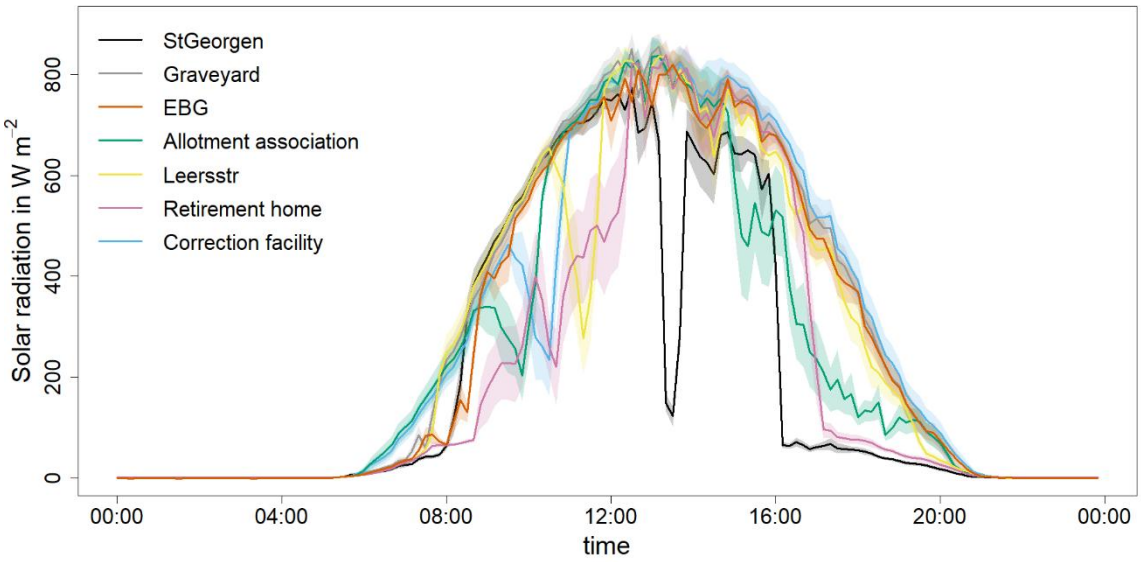

Figure 3.16: Mean diurnal course of solar radiation at the MWS for autochthonous days during the measurement period of July and August. Standard errors are visualised as polygons of the same colour.

To incorporate the wind field into the evaluation of temperature, humidity and energy flux patterns, wind vectors were determined along the measurement route for the three measurement rides (Figure 3.17 - Figure 3.19). The first two measurement rides were conducted during weak wind conditions of 0.7-0.8 m s^{-1} at the WA MWS. For the third measurement ride, winds were slightly elevated to 1 m s^{-1}. Wind channelling can be seen along the very densely built Brandenburger street and the St Georgen street. It is disturbed at intersections, especially the TP and lower between the intersections for the treelined Brandenburger street. Notably, the wider and more exposed Markgrafenallee doesn't show wind channelling. Wind speeds are reduced at the AA for all rides and elevated at the neighbouring more exposed CF, at least during the August measurement rides. At the RH, wind speed is higher, but the wind direction is subject to strong variation. For stronger north-westerly winds, wind speeds are also elevated in the WA, especially closer to the river in the east further away from the city body in the west (Figure 3.19). During these stronger winds, wind speeds are prominently reduced only for the south-western part of the district including the GY, the northern part of the Brandenburger street, the AA, and the high buildings residential area between AA and Markgrafenallee. The measurements confirm the classification of the measurement ride days as autochthonous in respect to the low wind conditions. The disturbances of the wind field at intersections emphasises the importance of choosing ride sections with no intersections for the EC transects.

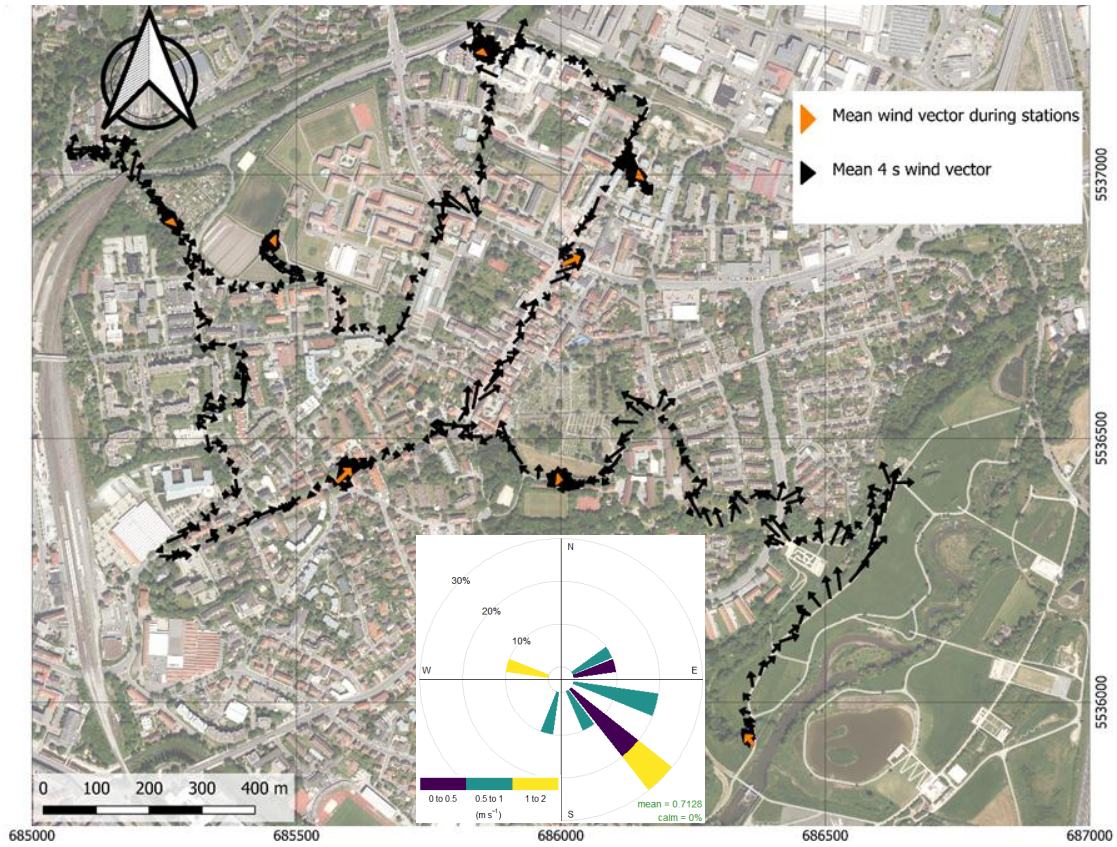

Figure 3.17: 4 s mean wind vectors during the mobile measurement ride on the 30th of July 16:12-17:00 CEST (map). Wind directions at the WA MWS during the same time interval are shown in the bottom centre plot. Map material was provided by the State Institute for Geodesy of Bavaria (Bayerische Vermessungsverwaltung, 2025).

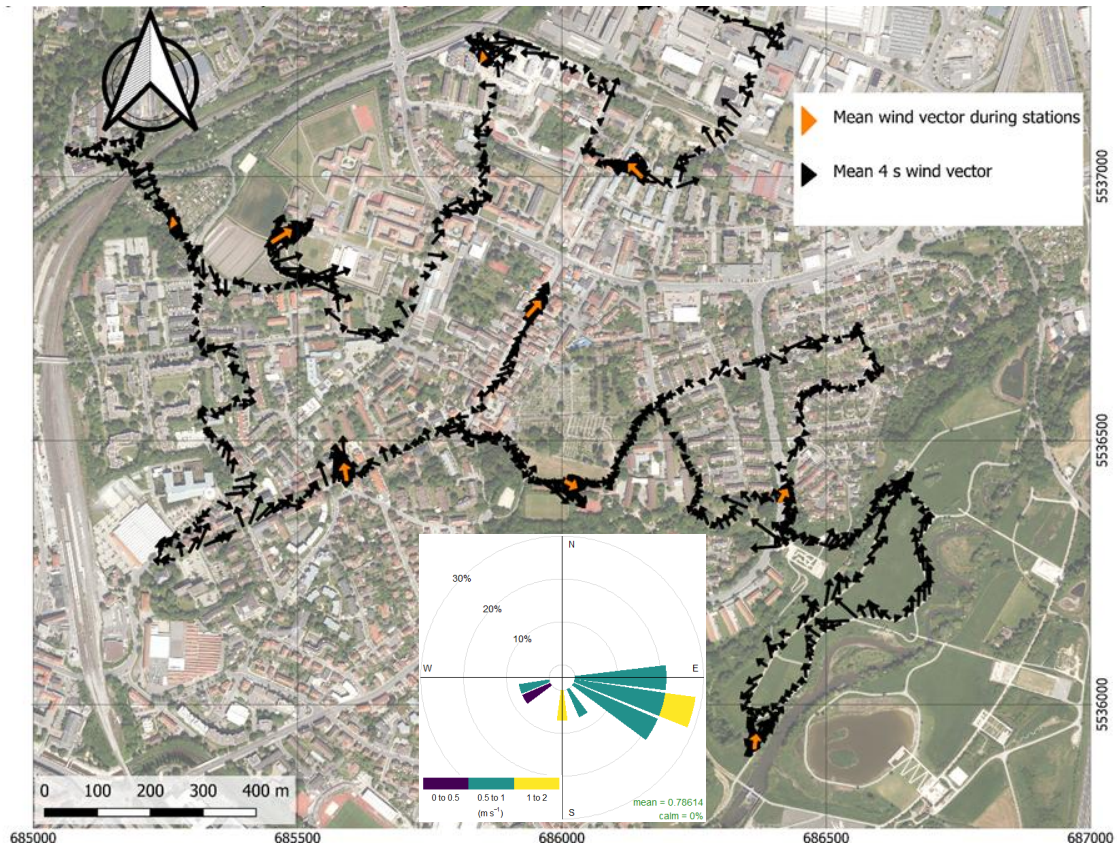

Figure 3.18: 4 s mean wind vectors during the mobile measurement ride on the 12th of August 16:19-17:30 CEST (map). Wind directions at the WA MWS during the same time interval are shown in the bottom centre plot. Map material was provided by the State Institute for Geodesy of Bavaria (Bayerische Vermessungsverwaltung, 2025).

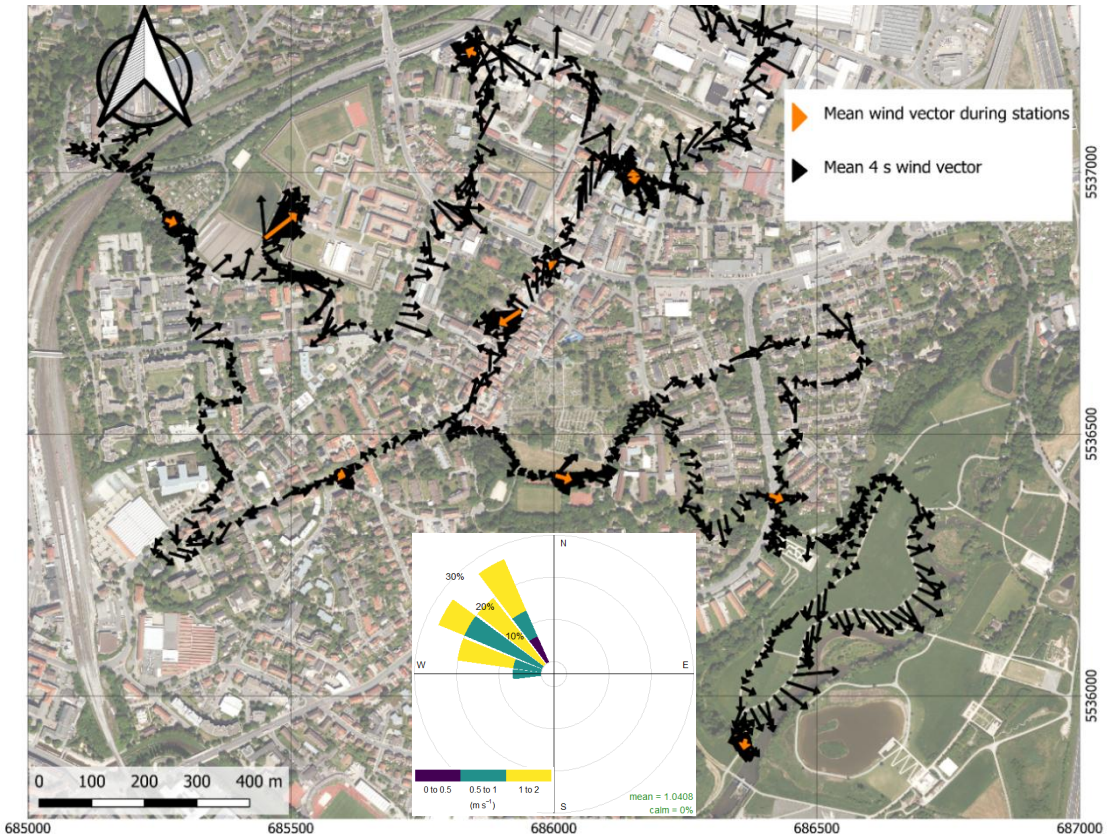

Figure 3.19: 4 s mean wind vectors during the mobile measurement ride on the 14th of August 17:00-18:15 CEST (map). Wind directions at the WA MWS during the same time interval are shown in the bottom centre plot. Map material was provided by the State Institute for Geodesy of Bavaria (Bayerische Vermessungsverwaltung, 2025).

4 Discussion

Preliminary discussions on the accomplished results were already conducted in chapter 3. In this chapter the presented results will be collated and put into context of findings in previous studies. Also, the proposed hypotheses will be assessed. Lastly the applied methods will be discussed.

4.1 Comprehensive discussion of results

In the St Georgen/ Burg district distinct microclimates formed in the urban canopy layer under autochthonous conditions in July and August. They partly established for scales smaller than the scale of local climate zones (LCZ's) as for the bikeway south of the GY, the AA bikeway, the LS MWS and the street east of the RH. It was shown that temperature and humidity can be influenced by effects distinct for the respective street canyon. Treelines along bikeways and small extents of urban building patterns make abstractions to a larger scale difficult. The effect of micro-scale urban climate variabilities was already found in a study on LCZ application in heterogenous urban terrain in Hongkong (Shi et al., 2018). Additionally, a systematic review of urban heat dynamics suggested the assessment of complex urban structures as one possible improvement to the LCZ approach (Rahmani and Sharifi, 2025), emphasising the importance of assessing climatic effects caused by unique surrounding structures. Urban microclimates are dependent on the available energy due to radiation and storage (chapter 1.2). With strong advective forces missing under low wind conditions, the microclimates are not disturbed in their formation keeping their distinct characteristics like T_{air} and e (Quanz et al., 2018). The available canopy layer energy budget is closely linked to the surrounding land use characteristics. Surface sealing limits the available water for evapotranspirative heating reduction, dark roads increase energy uptake from shortwave radiation, street canyons trap longwave radiation but provide shade over part of the diurnal course and traffic acts as an additional anthropogenic heat source. If the enhanced radiative energy uptake and trapping, anthropogenic heat and missing evapotranspirative cooling in urban areas aren't compensated by sufficient shading over the diurnal course, T_{air} values can even exceed those at unshaded rural sites. This is contrary to the theoretical case usually presented as textbook knowledge (Oke et al., 2017). At sites like the SG MWS, Markgrafenallee and the residence in the northeast of St Georgen/ Burg, T_{air} of around 0.5-1.5 K higher than in the rural reference EBG and WA could be observed during the afternoon heat peak. The Markgrafenallee and residential area possessed a rather open sky view with low adjacent buildings providing no sufficient shade. The SG site was less open but still wide and densely packed with 3-4 story buildings and equipped with a dark cobblestone road, increasing shortwave radiation uptake and radiative trapping. The shade of the buildings over the diurnal course wasn't sufficient to reduce afternoon T_{air} below T_{air} at the EBG and WA. A positive correlation between building area and T_{air} that

is stronger for lower buildings has also been observed in Osaka, Japan (Yoshida et al., 2020). Additionally, the rural references in this evaluation possessed adjacent trees (EBG) and open water (WA) that caused deviations from an “optimal” homogenous flat rural reference as defined by Oke (2017). Lastly, reduced solar radiation at ground level due to anthropogenic aerosols could be expected to play a minor role for a mid-sized city like Bayreuth.

Dense treelines could help reduce heat accumulation even for densely built areas, as seen in the Brandenburger street and the residential area in the west, between the Brandenburger street and the AA. Since the energy availability from shortwave radiation plays such an important role during the day, street orientations were shown to have an important impact as well. For example, the high buildings east of the RH provided sufficient shading for the northerly adjacent road, leading to a reduction in heat accumulation that exceeds the temperature reduction of the previously mentioned dense treelines. This dominant role of the solar radiation in forming microclimates was also found in Berlin in a study on micro-scale T_{air} variability (Quanz et al., 2018).

Temperature differences during the late afternoon transition cooling and the nighttime afterwards were dominantly caused by the heat capacity and diffusivity at a location. This can be seen in the close relation between decreasing building area and increasing cooling rates for the different MWS in the St Georgen/ Burg district (Figure 3.5). A closer look on nighttime perturbations of T_{air} is taken in Resch (2025).

Humidity perturbations were mostly caused by limited water availability due to surface sealing. This is shown by the strong predictive power of the linear regression model of e and land use (Figure 3.9). Due to the limited water availability and the previously described additional urban heating reduction mechanisms, e and thereby water availability, was a weak predictor for spatial T_{air} perturbations within the St Georgen/ Burg district (Figure 3.10). The mechanism of reduced heating due to evapotranspiration could only be applied when comparing urban and rural locations.

Turbulent energy fluxes during the afternoon heat peak showed strong dependencies on the local radiative energy budget, similar to those of the spatial T_{air} perturbations. Depending on the water availability, the positive energy fluxes had a bigger share of latent or sensible heat flux. Sufficient water availability enabled a dominance of energy transport via the latent heat flux, preventing heat retention in increased T_{air} within the urban canopy layer. The spatial patterns of turbulent energy flux magnitude and Bowen ratio as visualized in Figure 3.15, assess two fundamental factors of daytime urban canopy layer T_{air} patterns: Incoming shortwave radiation and water availability. The fundamental role of these two factors for the urban canopy layer energy balance has been established as textbook knowledge by Oke et al. (2017). As shortwave radiation and water availability are a direct consequence of surrounding land use under autochthonous conditions, turbulent energy fluxes can be used as an agent for land use impacts on energy budgets and provide a comprehensive base for explaining spatial T_{air} patterns.

For the diurnal course from noon to midnight, it was shown that heat retention in the urban district of St Georgen/ Burg is more efficient than in the rural reference sites WA and EBG. That implies a lower efficiency in heat dissipation for the urban sites. This, along with the previously described urban typical heat accumulation enhancements over the diurnal course, leads to higher maximum T_{air} and reduced late afternoon cooling rates. Dense treelines provided a small reduction in maximum T_{air}, that was exceeded by reductions due to shading in east-west oriented streets. The most effective reduction in T_{air} was achieved by dense aggregations of vegetation including trees and unsealed surfaces that enable water retention and evapotranspirative heating reduction (Figure 3.11).

4.2 Discussion of hypotheses

In this chapter, the hypotheses will be discussed based on the evaluation results in chapter 3 and discussions in chapter 3 and 4.1. Both research questions were already assessed in chapter 3. To assess the different parts of the hypotheses individually, they are divided into subsections and presented in italics.

Hypothesis 1a

*During the summer, the **land use distribution** is a strong **predictor** for spatial urban canopy layer **air temperature** and **absolute humidity** differences during autochthonous synoptic conditions.*

The land use distribution, as used in this thesis, was a sufficient predictor for spatial absolute humidity differences in form of e within the urban canopy layer of the St Georgen/ Burg district during autochthonous conditions. The same cannot be stated about its predictive power for spatial T_{air} differences. As the correlation between T_{air} and e is reduced when excluding rural sites from the analysis, so is the predictive power of the model. Relations between land use type and e boil down to surface sealing and share of vegetated areas. This makes the simple linear regression model approach with two-dimensional land use area shares sufficient. For the spatial T_{air} perturbations, more complex processes are at play that are not sufficiently represented in the two-dimensional linear regression model approach. These include the building height, street orientation, surface material and tree size. This part of the hypothesis can be rejected for the prediction of T_{air} but not for the prediction of e.

*For these conditions, an increase in the proportion of land covered by **buildings** and **pavement** compared to vegetation is **associated with higher air temperatures** and **lower absolute humidity**.*

Increased T_{air} could be partly attributed to a higher share of building areas compared to vegetation during the day and more during the night. Decreased e could be attributed to

increase in the proportion of land covered by buildings and pavement compared to vegetation during the afternoon. This part of the hypothesis cannot be rejected.

These existing temperature differences increase during the late afternoon transition.

T_{air} started deviating between the MWS during the late afternoon transition but was not in line with the existing temperature differences during the afternoon. For example, locations shaded by tree canopy simply show smaller diurnal temperature amplitudes than exposed vegetated locations. They have lower T_{air} during the day and smaller cooling rates in the late afternoon. This part of the hypothesis can be rejected.

Hypothesis 1b

Due to a lack of buildings as heat storage as well as shading and evapotranspirative heating reduction during the day, the formation of a ***park cool island*** *is expected in the* ***graveyard*** *southern meadow and the* ***allotment association*** *during autochthonous synoptic conditions throughout day and night*.

The GY southern meadow and the AA continuously showed reduced T_{air} compared to the other MWS locations in the St Georgen/ Burg district except for the period from morning to noon. During night, the temperatures were in-between the lower T_{air} at the EBG and the higher T_{air} at the other MWS locations. The latter findings reproduce the observation of the park cool island in a Bayreuth city centre park done by Isabel Spies (Spies, 2019). This hypothesis can be partially rejected as the PCI didn't establish for the whole diurnal course but only from noon to the next morning.

Hypothesis 2a

For autochthonous afternoons in the summer, the ***upward sensible heat flux*** *in the urban canopy layer is* ***increased*** *for higher proportions of land covered by* ***buildings*** *and* ***pavement*** *compared to vegetation*.

The upward sensible heat flux was mainly driven by available radiative energy. If the surrounding buildings didn't block the direct radiation, enhanced upward sensible heat fluxes were observed, for example at the SG-mobile transect, and attributed to trapping of radiation. Sealed surfaces like pavement and buildings could enhance the upward sensible heat flux compared to low vegetation, as they retained no available water for latent heat fluxes. However, for locations where the surrounding buildings shielded direct solar radiation from the location, the whole energy budget available for turbulent heat fluxes was reduced. This part of the hypothesis cannot be rejected. Comparisons between locations of similar exposition to direct radiation but differing land use characteristics should be further assessed.

*Therefore, it is expected to be **highest** for **densely built** main streets, **lower** for **residential areas** and **lowest** for rural **grassland/meadows**.*

The highest heat flux values were observed at the CF, the SG and the residential area in the northeast. The lowest were observed at the AA, the GY the WA floodplain meadow and the bikeway between WA and GY. The distinction between main streets, residential areas and rural areas did not apply as it fails to account for site specific parameters like treelines, street orientation and water availability. This part of the hypothesis can be rejected.

Hypothesis 2b

*Due to a lack of buildings as heat storage as well as shading and evapotranspirative heating reduction during the day, the formation of a **park cool island** is expected in the **graveyard** southern meadow and the **allotment association** during autochthonous synoptic conditions throughout day and night.*

The strong dependency of latent heat fluxes on the water availability was already discussed in this thesis. Vegetation including treelines and open water were the only land use types associated with increased latent heat fluxes. Water retention is usually reduced in urban areas due to surface sealing. The vegetated areas were the only land use types within the St Georgen/ Burg district, that provided sufficient amounts of water for increased latent heat fluxes. The latent heat fluxes were also limited by the radiative energy budget. In shaded areas, latent heat fluxes were reduced compared to more exposed areas. This caused the latent heat fluxes in the WA to be the highest. This part of the Hypothesis cannot be rejected.

*It is also significantly increased at the **graveyard** southern meadow bikeway and the **allotment association**.*

Latent heat fluxes at the GY southern meadow bikeway and the AA were partly elevated compared to the other MWS. Due to increased shading, the available energy and therefore the respective latent heat fluxes were lower than in the WA. This part of the Hypothesis cannot be rejected.

4.3 Critique of methods

In this chapter, flaws in the applied methods will be assessed and possible improvements will be suggested. Methods are discussed as one method per paragraph. The discussed methods include the conducted measurement campaign as well as the post processing.

Usage of the SmartFlux3 system caused some errors in data logging of gas analyzer and anemometer values. The system was not robust for mobile on-off operations. The usage

of more robust dataloggers like the CR6 data logger (Campbell Logan, UT USA) is recommended.

The correction of the time instationarity was done by using an inverse distance squares algorithm. The method accounts for different instationarity progressions at different measurement sites but assumes continuous gradients between the different sites that are not necessarily true to reality. As shown in this thesis, microclimates can establish at street canyon scale and differ distinctly depending on their surroundings. Using a MWS network with up to several 100 m distances misses these micro-scale differences in the instationarity correction. For future studies, the MWS network setup should include all distinct land use types along the route or a different correction algorithm should be found.

The area of influence around the measurement locations was determined using the internal boundary layer concept. As this concept describes the downwind influence of abrupt changes in the surface properties, it is not applicable for this purpose from a physical basis. Since the development of distinct microclimates within the urban canopy layer could be explained through effects of the immediate surroundings on the energy budget, the internal boundary layer concept still worked as an approximation for the applications in this thesis. For future studies, the implementation of LES models, previously applied in Bayreuth by Sungur et al. (2025), could help implementing advection into the analysis.

The evaluation of the mobile T_{air} and e data was done using spatial averages. This led to high differences in the data volume, emphasised by the missing parts in two of the three measurement rides. Spatial averaging is useful to reduce influence of stochastic effects like closely passing cars. A bigger number of full ride datasets would improve reduction of stochasticity and reduce the differences due to different data volume.

The applied linear regression land use model ultimately failed in predicting spatial T_{air} perturbations within the St. Georgen/ Burg district. The two-dimensional model didn't account for the complexity of the urban structure. Since the model was promising in the prediction of water vapor perturbations, it seems mostly applicable for predicting evapotranspirative heating reduction. Additional factors that account for other sources of heating reduction should be implemented for future use. The sky view factor, detectable with a fisheye camera (Liu et al., 2017), or the aspect ratio of a street canyon retrieved via additional building height data (Oke et al., 2017) can account for additional effects of shading and radiative trapping. Lastly, the street orientation could be retrieved from the real time INS data recorded during the ride. These improvements could also be implemented with the help of an LES model, like the one used by Sungur et al. (2025). The close relationship between building area and T_{air} perturbation recorded at the MWS during nighttime makes the model seem more applicable for nighttime application, when complexity is reduced due to missing shortwave radiation exchange.

The approximation of defined street transects as homogenous areas that provide approximately steady state conditions had several flaws. Firstly, they were, by their nature, not open spaced as would be best practice for calculation of energy balances (Foken, 2017). Secondly, the transects were never fully homogonous due to differences in adjacent houses or gardens and parking cars. As the mobile EC measurements provide spatiotemporal averages (Mahrt, 1997), these inhomogeneities can also be interpreted as violations to the steady state assumption. Thirdly, unsteady elements like pedestrians or moving cars also violated steady state conditions as they rarely kept their relative position to the MobiFast measurement point. Lastly, it was difficult to find long enough transects that are undisturbed by crossing streets. This emphasises the limitation of the method to only enable comparative claims. Slower ride speeds, in-situ identification of possible transects and active avoidance of unsteady elements could enhance data quality for future studies.

The flux measurements along defined transects are subject to the risk of random error, as only one latent and sensible heat flux is measured for every transect during every ride. Repeated transect rides during single measurement rides would enable the evaluation of a whole spectrum of heat flux densities for the different days. This idea has already been established for flight operated EC measurements (Desjardins et al., 1989; Sun and Mahrt, 1994). The repeated transect measurements would also provide the opportunity to compare days of approximately similar synoptic conditions in their heat flux spectrum for the defined transects. All three stations at which mobile and stationary measurements were performed show a distinct tendency towards higher TKE for the mobile measurements. At first it should be mentioned, that TKE scales with turbulent wind speed squared, making it highly responsive even to small increases of that turbulent wind speed. Problems in mobile EC systems in general can arise from multiple sources as summarized by MAHRT (1997): The covered surface area of the mobile measurements always deviates from the stationary reference. This is especially the case for the SG MWS, where the MWS is shaded during the afternoon while the other side of the street isn't. The mobile measurements contain an additional dimension along the transect. They are a spatiotemporal mean value instead of a temporal mean like for stationary measurements. Lastly, a bigger sample size for mobile measurements can be expected, as the mobile device is moved through the turbulence, covering a bigger number of turbulent eddies. The same tendency could be partially identified for the turbulent energy fluxes at the three MWS where adjacent mobile and stationary EC measurements were performed. Test comparisons for multiple stationary and mobile EC measurements at a single transect could be performed to further investigate this tendency. Until further assessment, the presented TKE and turbulent energy fluxes should be interpreted with caution.

5 Conclusion

In this thesis, spatial high-resolution T_{air} and humidity perturbation patterns were detected within the urban canopy layer of St Georgen/ Burg during the afternoon heat peak. The patterns were set into context with turbulent energy fluxes, diurnal courses and land use data. Application of a nonparametric model was assessed for prediction of these patterns using polygon land use maps. For the underlying measurement campaign, a new system was set up to enable mobile EC measurements within the urban canopy layer.

The humidity perturbation patterns were found to be closely linked to surrounding land use and the applied model showed high predictive power. Evapotranspirative heating reduction within the district lacked behind the reduction potential found in the Wilhelminenaue floodplain meadow. T_{air} perturbation patterns could also be identified as land use driven, but the model showed low predictive power here. It failed in accounting for the complexity of urban-atmosphere interactions that shape the urban canopy layer's T_{air} perturbations. The model seemed capable of detecting below LCZ level differences during autochthonous synoptic conditions but needs to be adjusted before further usage on T_{air} perturbations according to the suggestions made in chapter 4.3. Implementation of the sky view factor, building height and street orientation were suggested as possible improvements. Usage of LES models could help implementing effects of advection. Treelines were found to reduce heating in the urban canopy layer during the afternoon heat peak. However, their reduction effectivity was succeeded by heating reduction due to shading from high buildings. To achieve a cooling relative to the whole temperature distribution within the district, a high aggregation of vegetation was needed, like it is found in parks. Parks provided reduced temperatures from noon to midnight, diminishing heat stress during the warmest time of the day and working towards UHI reduction during night, when the effect is most prominent. The applicability of the mobile EC measurement method was shown, though it is limited to comparative claims. The method needs to be tested further but showed promising results as being an agent for underlying processes, shaping urban temperature and humidity perturbation patterns.

The main objective of this thesis, to identify spatial high resolution T_{air} and humidity perturbation patterns within the urban canopy layer during the afternoon heat peak and determine their origin in the exchange of energy between atmosphere and urban surfaces as radiation and turbulent fluxes, was met. The understanding of these energy exchange processes in the urban canopy layer was enhanced. The determined T_{air} and humidity perturbation patterns can be used for heat mitigation strategies. The discussed underlying principles provide a base for future city development. Increasing water retention by land unsealing and providing sufficient shading can increase citizens' comfort during thermally stressful times of the day. Preserving and maintaining parks offers evasion opportunities for vulnerable groups. The feedback processes between the city body and the available energy within the urban canopy layer during the day should be thoroughly taken into account for future research and city development.

6 Acknowledgments

First and foremost, I'd like to thank Prof. Dr. Christoph Thomas for providing the framework that enabled me to write this thesis and conduct the underlying measurement campaign. With his theoretical introductions I could develop an understanding of urban climate phenomena, meteorologic data acquisition and handling, and especially turbulent energy fluxes. His ideas, support and feedback made the successful measurement campaign and completion of this thesis possible. He also provided me his self-written processing tool "bmmflux" for post processing the mobile-measured climate elements and calculating turbulent energy fluxes and turbulence statistics. Special thanks go also to Johannes Olesch who took care of the nuts and bolts in assembling the MobiFast setup. I thank him and Markus Friedrich for the support in installing the additional MWS in the St Georgen/ Burg district. I'd like to thank Dr. Wolfgang Babel for his support with IT and programming related questions. I also thank him, Prof. Dr. Christoph Thomas and the whole Micrometeorology group for their constructive feedback on my presentations at our biweekly meeting. A big thank you goes out to Florian, Michi, Insa and the whole ATMOS-team for keeping my sanity during the writing process on board of the Polarstern. Lastly, I thank my dear colleague and friend Sophie Resch for her collaboration on the measurement campaign, and for her continuous support and role as a first responder to any major and minor questions and emergencies concerning this thesis.

7 Bibliography

Aslam, A.; Rana, I. A. (2022): The use of local climate zones in the urban environment: A systematic review of data sources, methods, and themes. In *Urban Climate* 42, p. 101120. DOI: 10.1016/j.uclim.2022.101120.

Aubinet, M.; Vesala, T.; Papale, D. (2012): Eddy Covariance. Dordrecht: Springer Netherlands.

Bayerische Vermessungsverwaltung (2025). Edited by © Bayerische Vermessungsverwaltung. © Bayerische Vermessungsverwaltung. Geoportal Bayern. Available online at www.geoportal.bayern.de.

Bechtel, B.; Demuzere, M.; Mills, G.; Zhan, W.; Sismanidis, P.; Small, C.; Voogt, J. (2019): SUHI analysis using Local Climate Zones—A comparison of 50 cities. In *Urban Climate* 28, p. 100451. DOI: 10.1016/j.uclim.2019.01.005.

Bundesinstitut für Bau-, Stadt- und Raumforschung (Ed.) (2023): Die Entwicklung der Städte und Gemeinden in Deutschland. Bundesamt für Bauwesen und Raumordnung (BBR). Available online at https://www.bbsr.bund.de/BBSR/DE/daten-karten/raumentwicklung/2025/entwicklung-staedte-gemeinden-dashboard-html.html, checked on 8/15/2025.

Cardoso, R. S.; Amorim, M. C. C. T. (2018): Urban heat island analysis using the 'local climate zone' scheme in Presidente Prudente, Brazil. In *Ingeo* (69), p. 107. DOI: 10.14198/INGEO2018.69.07.

Desjardins, R. L.; Macpherson; J. I.; Schuepp, P. H.; Karanja, F. (1989): An evaluation of aircraft flux measurements of CO 2, water vapor and sensible heat. In *Boundary-Layer Meteorology* (47), pp. 55–69.

Dodman, D.; Hayward, B.; Pelling, M.; Broto, V. C.; Chow, W.; Chu, E. et al. (2022): Climate Change 2022 – Impacts, Adaptation and Vulnerability. Contribution of Working Group II to the Sixth Assessment Report of the Intergovernmental Panel on Climate Change [H.-O. Pörtner, D.C. Roberts, M. Tignor, E.S. Poloczanska, K. Mintenbeck, A. Alegría, M. Craig, S. Langsdorf, S. Löschke, V. Möller, A. Okem, B. Rama (eds.)]. In *Assessment Report of the Intergovernmental Panel on Climate Change* (6), pp. 907–1040. DOI: 10.1017/9781009325844.

DWD (2025a): Heißer Tag. Wetter- und Klimalexikon. Edited by Deutscher Wetterdienst. Bundesbehörde im Bundesministerium für Verkehr. Available online at https://www.dwd.de/DE/service/lexikon/Functions/glossar.html?lv3=101162&lv2=101094, checked on 9/11/2025.

DWD (2025b): Rückblick auf den globalen Niederschlag in 2024. Pressemitteilung zum Weltwassertag am 22. März 2025. Edited by Deutscher Wetterdienst. Bundesbehörde im Bundesministerium für Verkehr. Available online at

https://www.dwd.de/DE/presse/pressemitteilungen/DE/2025/20250320_pm_weltwasserrtag_2025_news.html, checked on 9/11/2025.

Foken, T. (2017): Micrometeorology. Chapters 3.2, 4.2. Berlin, Heidelberg: Springer Berlin Heidelberg.

Kaimal, J. C.; Gaynor, J. E. (1991): Another look at sonic thermometry. In *Research note* (56), pp. 401–410.

Kousis, I.; Manni, M.; Pisello, A. L. (2022): Environmental mobile monitoring of urban microclimates: A review. In *Renewable and Sustainable Energy Reviews* 169, p. 112847. DOI: 10.1016/j.rser.2022.112847.

Leconte, F.; Bouyer, J.; Claverie, R.; Pétrissans, M. (2015): Using Local Climate Zone scheme for UHI assessment: Evaluation of the method using mobile measurements. In *Building and Environment* 83, pp. 39–49. DOI: 10.1016/j.buildenv.2014.05.005.

Lehnerta, M.; Kubeček, J.; Geletič, J.; Jurek, M.; Frajer, J. (2018): Identifying hot and cool spots in the city centre based on bicycle measurements: The case of Olomouc, Czech Republic. In *Geographica Pannonica* 22 (4), pp. 230–240. DOI: 10.5937/gp22-19750.

Liu, L.; Lin, Y.; Liu, J.; Wang, L.; Wang, D.; Shui, T. et al. (2017): Analysis of local-scale urban heat island characteristics using an integrated method of mobile measurement and GIS-based spatial interpolation. In *Building and Environment* 117, pp. 191–207. DOI: 10.1016/j.buildenv.2017.03.013.

Mahrt, L. (1997): Flux Sampling Errors for Aircraft and Towers. College of Oceanic and Atmospheric Sciences, Oregon State University, Corvallis, Oregon. In *JOURNAL OF ATMOSPHERIC AND OCEANIC TECHNOLOGY* (15), Article 416-429.

Malberg, H. (2007): Meteorologie und Klimatologie Einführung. Eine Einführung. Chapter 15. 5th ed.: Springer Berlin Heidelberg.

Mills, G. (2008): Luke Howard and The Climate of London. In *Weather* 63 (6), pp. 153–157. DOI: 10.1002/wea.195.

Moore, C. J. (1986): Frequency response corrections for eddy correlation systems. In *Boundary-Layer Meteorol* (37), pp. 17–35.

Oke, T. R.; Mills, G.; Christen, A.; Voogt, J. A. (Eds.) (2017): Urban Climates: Cambridge University Press.

Quanz, J.; Ulrich, S.; Fenner, D.; Holtmann, A.; Eimermacher, J. (2018): Micro-Scale Variability of Air Temperature within a Local Climate Zone in Berlin, Germany, during Summer. In *Climate* 6 (1), p. 5. DOI: 10.3390/cli6010005.

Raabe, A.; Foken, T. (2003): Die Höhe der internen Grenzschicht im Windfeld nach einer sprunghaften Änderung der aerodynamischen Rauhigkeit der Unterlage - Beispiel Küste. In *Beiträge zur Klima- und Meeresforschung*, pp. 227–237.

Rahmani, N.; Sharifi, A. (2025): Urban heat dynamics in Local Climate Zones (LCZs): A systematic review. In *Building and Environment* 267, p. 112225. DOI: 10.1016/j.buildenv.2024.112225.

Resch, S. (2025): Characterizing summer nighttime urban heat island intensity and cold-air dynamics through mobile flux measurements and stationary sensor networks in a mid-sized city in central Europe. Bachelor Thesis. University of Bayreuth, Bayreuth. Micrometeorology group.

Schappacher, O. (2024): Analyse der Ausprägung des Mikroklimas im Bayreuther Süden mithilfe von stationären und mobilen Messungen. Bachelor Thesis. University of Bayreuth, Bayreuth. Micrometeorology group.

Schotanus, P.; Nieuwstadt, F.T.M.; Bruin, H.A.R. (1983): Temperature measurement with a sonic anemometer and its application to heat and moisture fluxes. In *Boundary-Layer Meteorol* 26 (1), pp. 81–93. DOI: 10.1007/BF00164332.

Shi, Y.; Lau, K. K.; Ren, C.; Ng, E. (2018): Evaluating the local climate zone classification in high-density heterogeneous urban environment using mobile measurement. In *Urban Climate* 25, pp. 167–186. DOI: 10.1016/j.uclim.2018.07.001.

Spaete, E. (2023): Simulating an extreme heat event in a mid-sized city in Europe with Large Eddy Simulation: investigating the impact of spatial resolution and validation with an observation network. Masters thesis. University of Bayreuth, Bayreuth. Micrometeorology group.

Spies, I. (2019): Urban climate - just warm streets and cool parks? Investigating the variabilities of heat at street-canyon and city-wide scale in Bayreuth. Master Thesis. University of Bayreuth, Bayreuth. Micrometeorology group.

Stadt Bayreuth (2025): Hitzeschutz-Strategie. Demografiefeste Kommune. With assistance of B.A.U.M. Consult. Available online at https://www.bayreuth.de/rathaus-buergerservice/planen-bauen/konzepte/hitzeanpassungsstrategie/ (08.09.2025).

Stewart, I. D.; Oke, T. R. (2012): Local Climate Zones for Urban Temperature Studies. In *Bulletin of the American Meteorological Society* 93 (12), pp. 1879–1900. DOI: 10.1175/BAMS-D-11-00019.1.

Sun, J.; Mahrt, L. (1994): Spatial Distribution of Surface Fluxes Estimated from Remotely Sensed Variables. In *Journal of Applied Meteorology and Climatology* (33), pp. 1341–1353.

Sungur, L. (2021): Mitigating heat accumulation in a mid-size urban area. Applying micrometeorological flow-resolving simulations to assess climate effects of urban planning measures. Master Thesis. University of Bayreuth, Bayreuth. Micrometeorology group.

Sungur, L.; Babel, W.; Späte, E.; Schneider, J.; Thomas, C. K. (2025): Climate sensitive designs for policy makers: How LES model resolution affects accuracy in capturing

urban micro-scale weather during heatwaves. In *Urban Climate* 61, p. 102400. DOI: 10.1016/j.uclim.2025.102400.

Thomas, C. K. (2025): Monatswerte Niederschlag und Temperatur. Mikrometeorologie; Universität Bayreuth. Fakultät für Biologie, Chemie und Geowissenschaften. Available online at https://www.bayceer.uni-bayreuth.de/meteo/de/klimastati/gru/html.php?id_obj=140009, checked on 9/11/2025.

Thomas, C. K.; Samimi, C. (Eds.) (2021): Schlussbericht Forschungsvorhaben: Minderung Städtischer Klima- und OzonRisiken (MiSKOR). Verbundprojekt „Klimawandel und Gesundheit“. Schlussbericht zum Forschungsvorhaben. With assistance of Prof. Dr. Christoph Thomas, Prof. Dr. Cyrus Samimi, Dr. habil. Johannes Lüers, Dr. Seyed Omid Nabavi, Prof. Dr. Anke Nölscher, Prof. Dr. Andreas Held. Universität Bayreuth.

Tschuschke A. (2019): Einfluss von Topografie, Fließgewässern und Bebauung auf die Temperaturverteilung und Luftströme im Bayreuther Becken. Analyse von fahrradgetragenen Messungen und Stationsdaten des MiSKOR-Messnetzes im Sommer 2019 Andreas Tschuschke. Bachelor Thesis. University of Bayreuth, Bayreuth. Micrometeorology group.

Valle, D.; Mintz, J.; Brack, I. V. (2024): Estimation and interpretation problems and solutions when using proportion covariates in linear regression models. Statistical Report. In *Ecology* 105 (4), e4256. DOI: 10.1002/ecy.4256.

Webb, E. K.; Pearman, G. I.; Leuning, R. (1980): Correction of flux measurements for density effects due to heat and water vapour transfer. In *Quart J Royal Meteoro Soc* 106 (447), pp. 85–100. DOI: 10.1002/qj.49710644707.

Yoshida, A.; Yasuda, R.; Kinoshita, S. (2020): Mobile Observation of Air Temperature and Humidity Distributions under Summer Sea Breezes in the Central Area of Osaka City. In *Atmosphere* 11 (11), p. 1234. DOI: 10.3390/atmos11111234.

Žgela, M.; Lozuk, J.; Jureša, P.; Justić, K.; Popović, M.; Boras, M.; Herceg-Bulić, I. (2024): Urban heat load assessment in Zagreb, Croatia: a multi-scale analysis using mobile measurement and satellite imagery. In *Environmental monitoring and assessment* 196 (5), p. 410. DOI: 10.1007/s10661-024-12538-w.

Zhang, S.; Breitner, S.; Donato, F.'; Stafoggia, M.; Nikolaou, N.; Aunan, K. et al. (2024): Heat and cause-specific cardiopulmonary mortality in Germany: a case-crossover study using small-area assessment. In *The Lancet regional health. Europe* 46, p. 101049. DOI: 10.1016/j.lanepe.2024.101049.

8 Appendix

The figures presented in this chapter are supportive for statements made and figures shown in the main thesis and contain additional information or visualisation for interested readers. First, a visualisation of the radiation night and windy day classification margin determination is shown (Figure 8.1), corresponding to Figure 2.5. Afterwards, the biases of the MWS solar radiation, T_{air} and e values, discussed in chapter 2.3.6, are visualized (Figure 8.2, Figure 8.3, Figure 8.4).

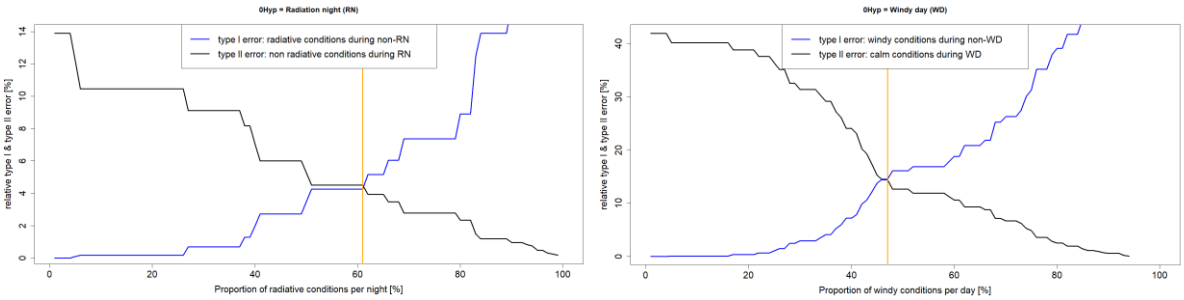

Figure 8.1: Visualization of the type I and type II error for classification of whole days as being followed by a radiation night (left) and as being windy days (right).

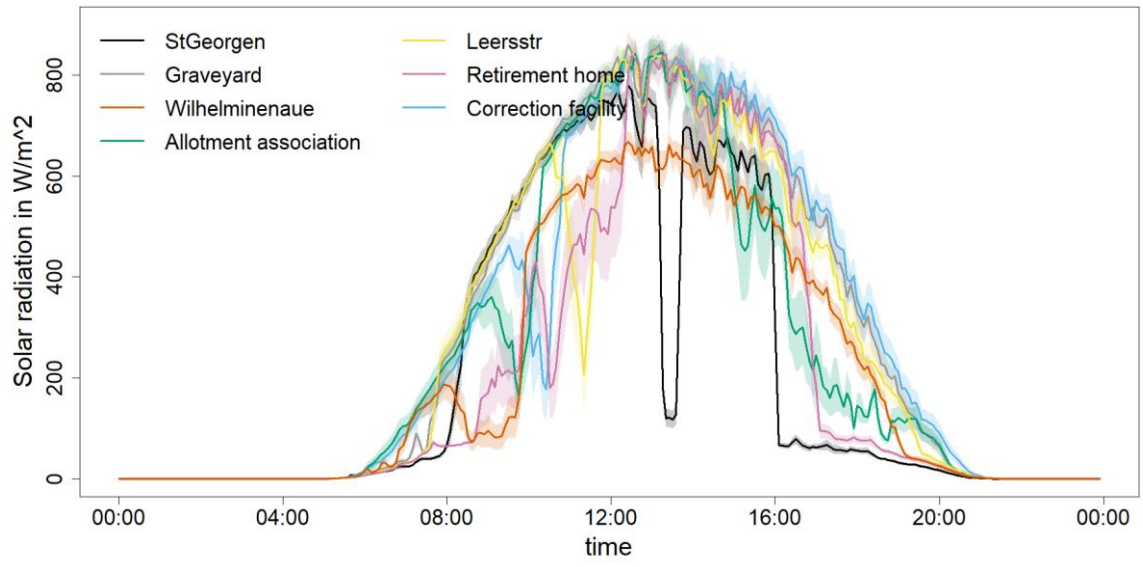

Figure 8.2: Mean diurnal course of solar radiation for autochthonous days (9) including the WA MWS instead of the EBG.

Additionally, four plots are shown putting the autochthonous diurnal progressions of T_{air} and e from chapter 3.1 into context with the allochthonous diurnal progressions (Figure 8.5, Figure 8.6, Figure 8.7, Figure 8.8). Also, the mean diurnal course of solar radiation during allochthonous conditions is shown (Figure 8.9), corresponding to Figure 3.16. As addition to Figure 3.11, a heatmap is shown, containing the results on pairwise t-tests between the 10 bins of vegetation area share (Figure 8.10). For comparison to

Schappacher (2024), a plot is presented showing the MWS data distribution of the autochthonous days used in this thesis for the radiation night criteria of gust speed below 2.2 m s^{-1} at the Mistel MWS and a T_{air}-difference of at least 2 K between Mistel and Kaemmerei MWS (Figure 8.11).

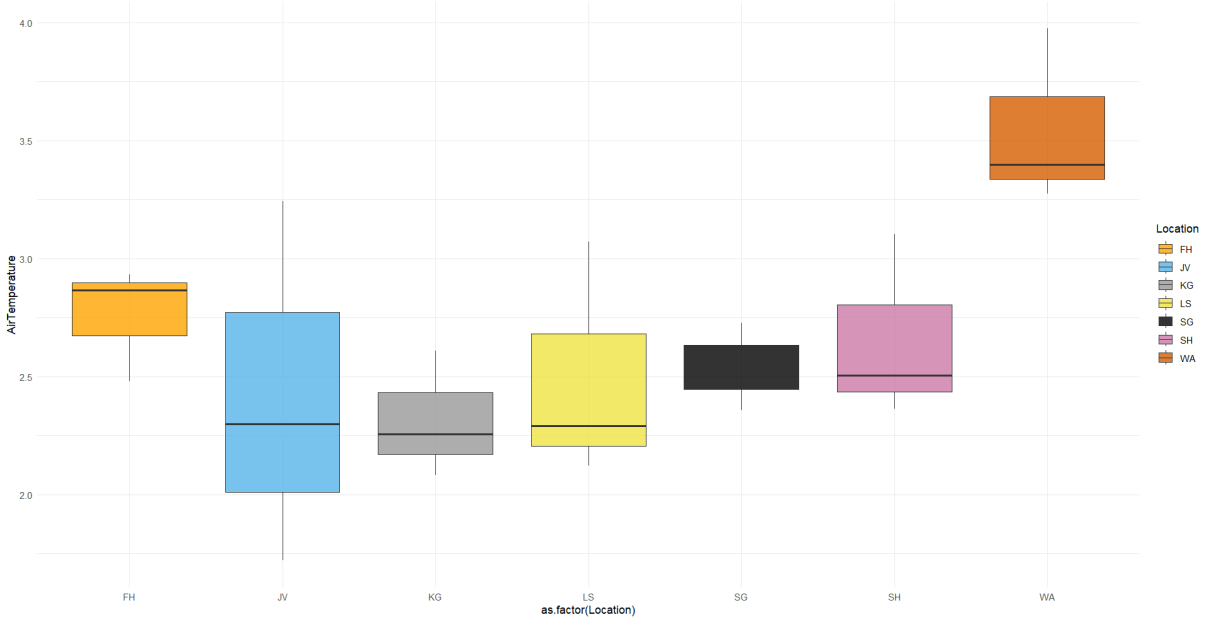

Figure 8.3: Bias in T_{air} [K] of the MWS relative to the MobiFast data during the 2-minute stops. The bias at the GY is increased by its placement on the GY southern meadow, while the stop was performed at the southerly adjacent treelined bikeway.

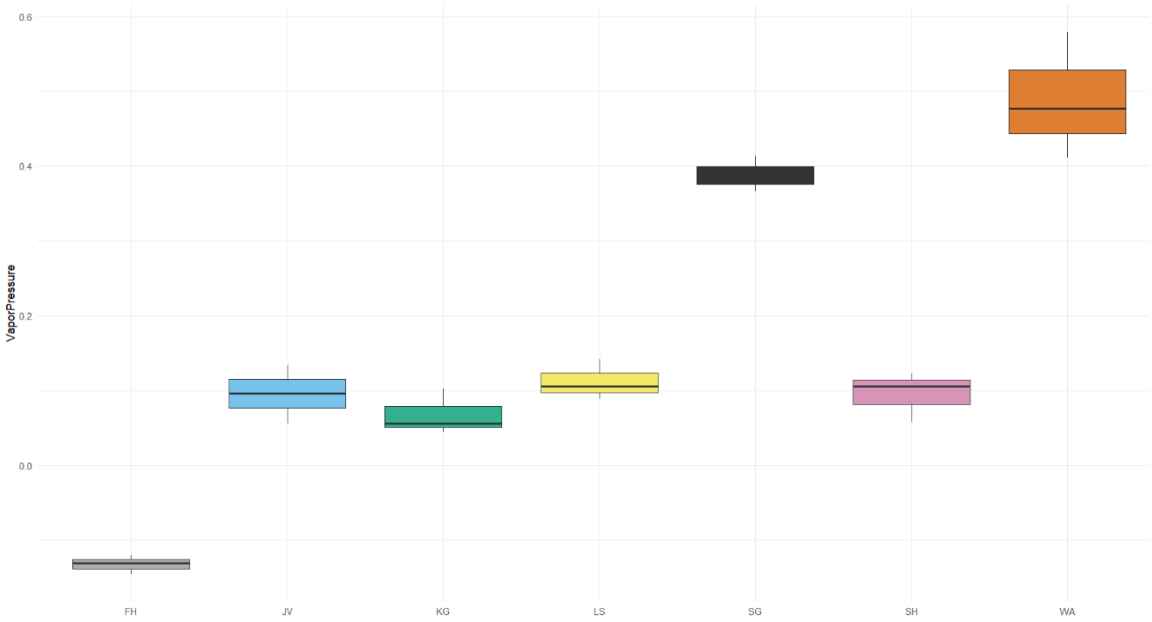

Figure 8.4: Bias in e [kPa] of the MWS relative to the Mobifast data during the 2-minute stops.

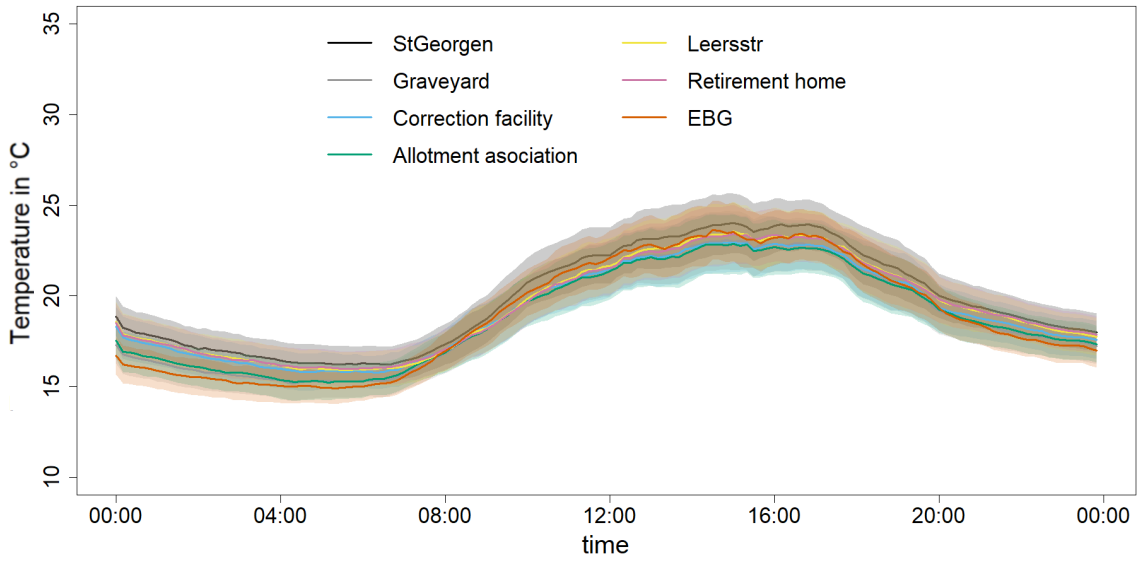

Figure 8.5: T_{air} in °C for allochthonous days (8) with standard error.

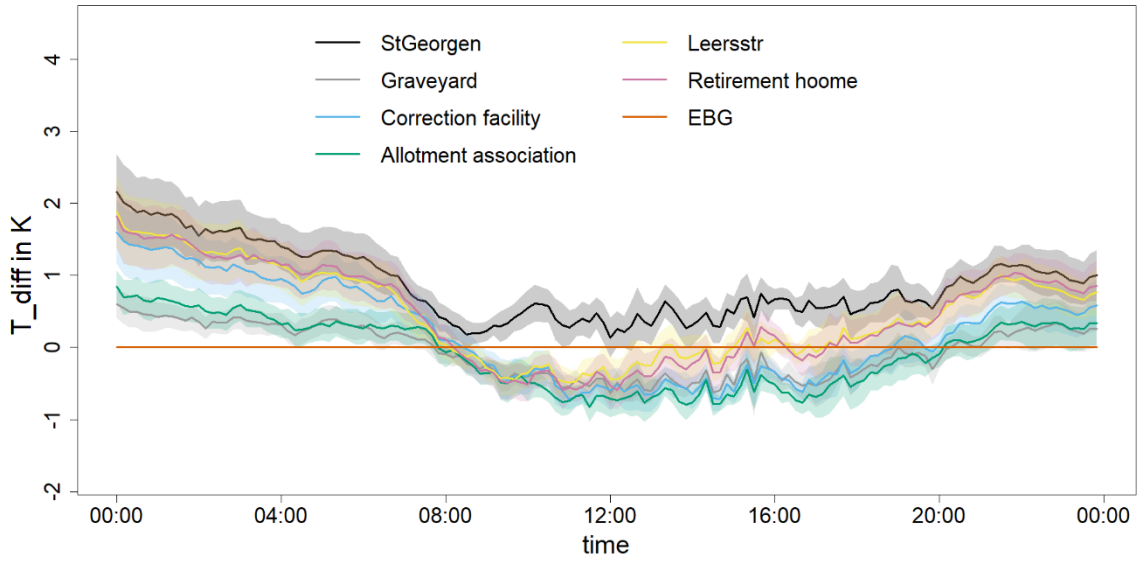

Figure 8.6: Difference of T_{air} relative to the EBG station in °C for allochthonous days (8) with standard error.

Lastly the data distributions of the corrected mobile T_{air} and e perturbations are shown (Figure 8.12). The visualisation includes q-q-plots and histograms for the three measurement rides conducted on July 30 and August 12 and 14. The shown values were aggregated as spatial averages for the perturbation maps and the land use model assessment in chapter 3.2. A summary of the linear regression land use models presented in chapter 3.2 is given at page 58 f.

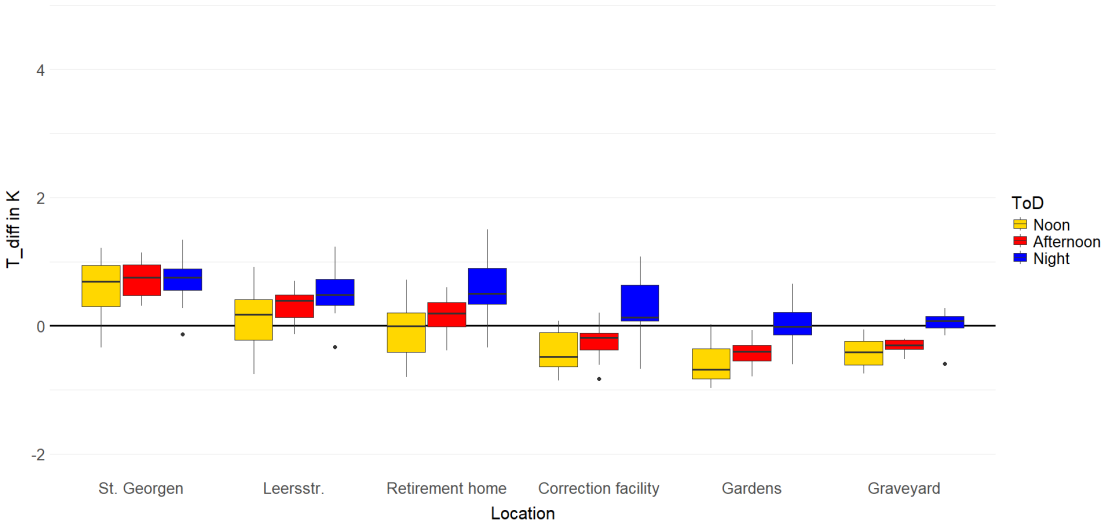

Figure 8.7: Difference of T_{air} relative to the EBG station in °C for allochthonous days (8) with standard error visualized as boxplots for hourly means during noon, the afternoon heat peak and the last hour of the day.

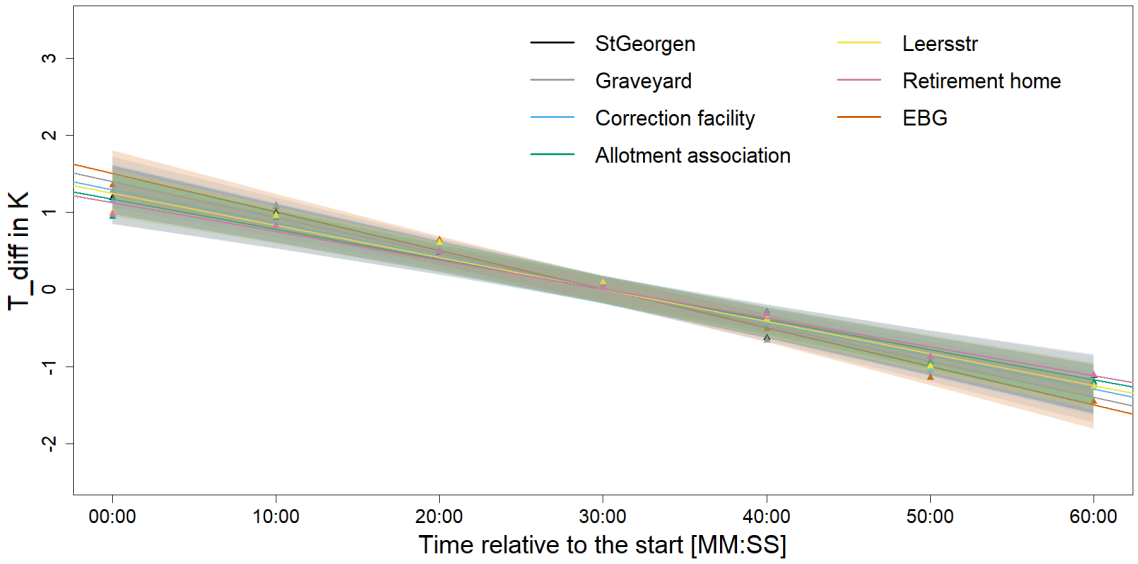

Figure 8.8: Mean relative T_{air} development for the six measurement locations and the EBG reference during the late afternoon transition (LAT) of the eight allochthonous days with linear models.

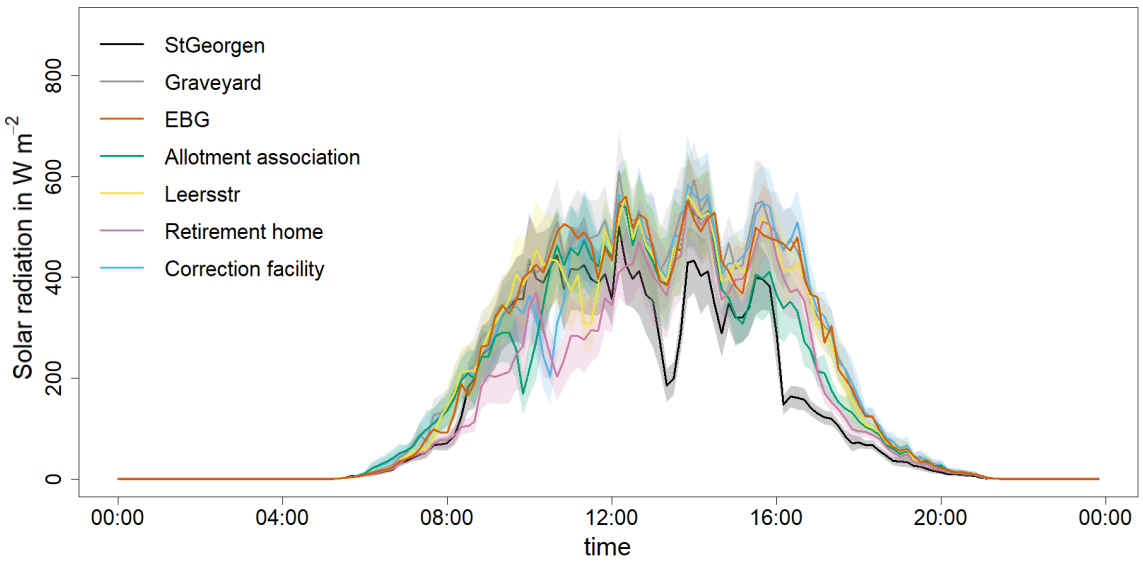

Figure 8.9: Mean diurnal course of solar radiation for allochthonous days (8) with standard error.

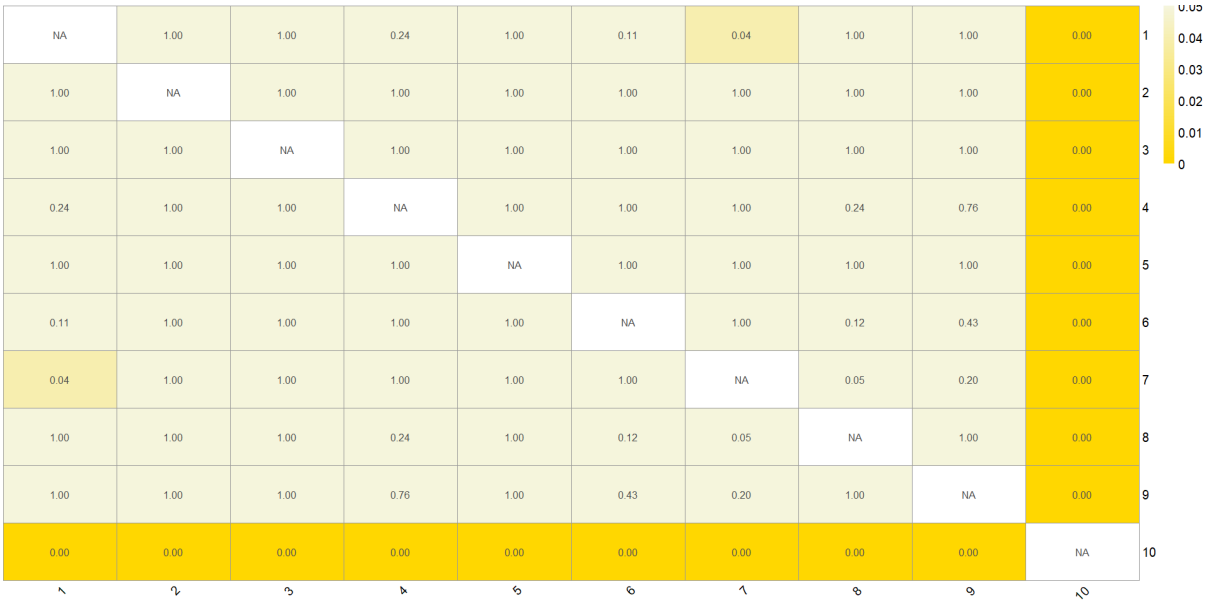

Figure 8.10: Pairwise t.test p-values across 10 bins of vegetation area share after Holm correction. The tested values were the spatial means of T_{air} perturbation (Mean Tdiff) during the three measurement rides without the WA

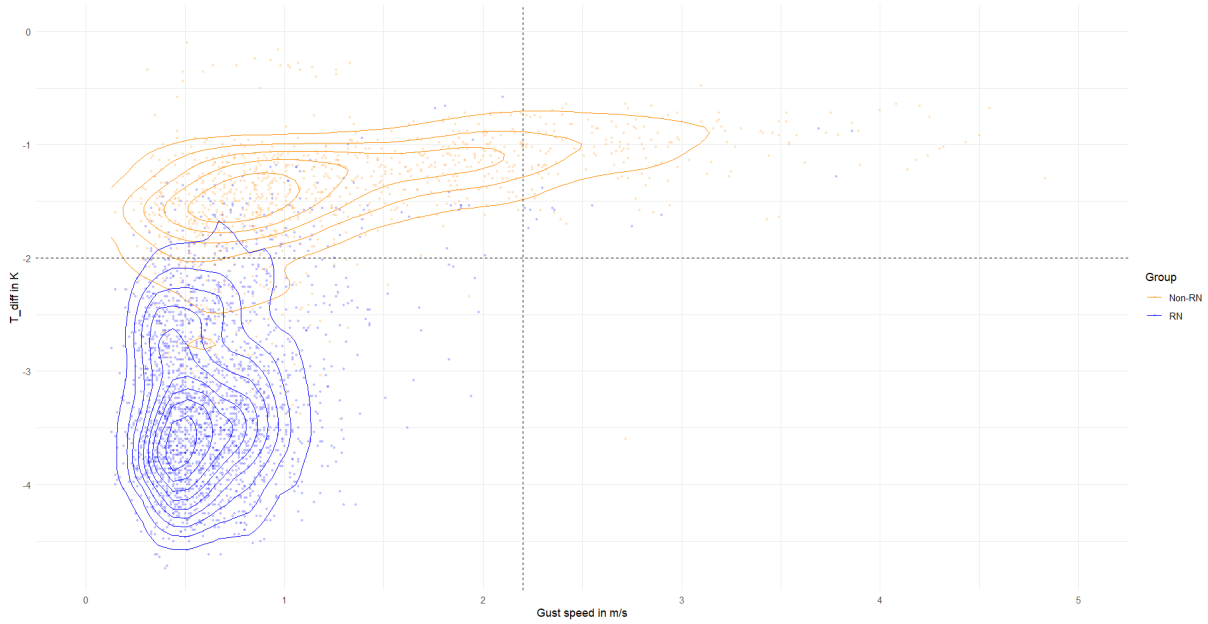

Figure 8.11: Temperature difference between Mistel and Kaemmerei vs gust speed at Mistel during nighttime. The plot is divided by the two criteria for cold air nights as defined by (Schappacher, 2024): A temperature difference > 2 K (here < -2 K) and agust speed < 2.2 m s^{-1} The plot is designed after Schappacher, 2024.

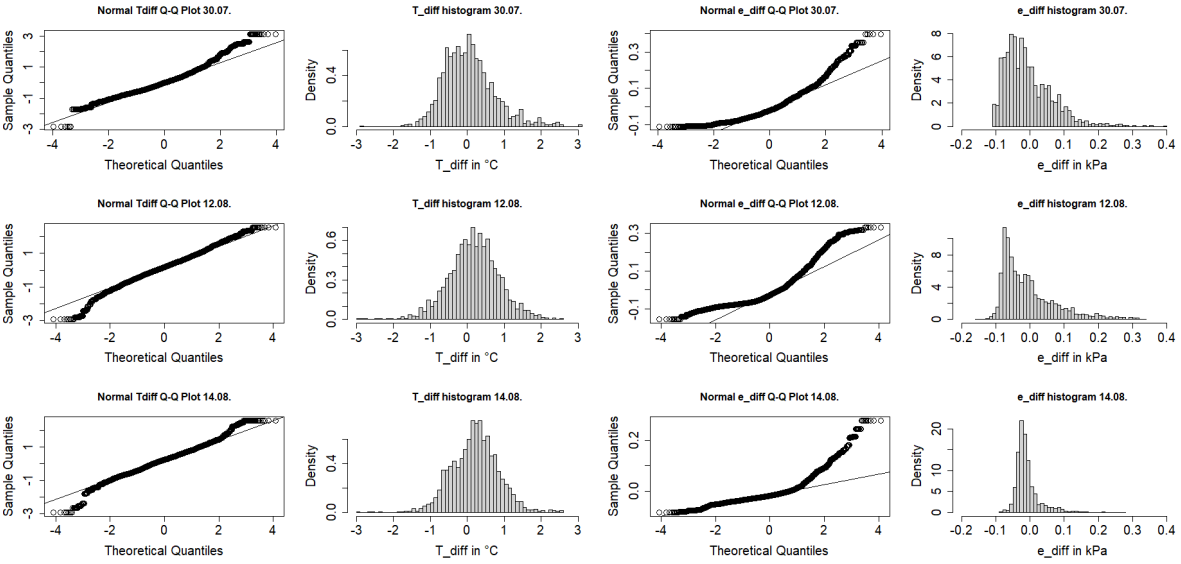

Figure 8.12: Overview of the ride data spatial T_{air} and e differences as Q-Q normal plots and histograms. The temperature perturbations show a normal distribution, and the e perturbation show right skewed distributions.

Summary of the linear regression models

Here, a summary of the linear regression models used for correlation of land use with spatial T_{air} and e perturbations is shown as presented in R. The four models are summarized individually. Model visualizations can be found in chapter 3.2.

a) T_{air} perturbation vs land use including Wilhelminenaue

```
lm(formula = mean_Tdiff ~ mean_NumTrees + mean_pavement + mean_low_vegetation +
  mean_high_vegetation + mean_water, data = df2_slim) # Mit WHM
Residuals:
   Min     1Q  Median     3Q     Max
-1.30855 -0.28269  0.00565  0.27729  1.31371
Coefficients:
                    Estimate Std. Error t value Pr(>|t|)
(Intercept)                  1.1598586  0.1143440  10.144  < 2e-16 ***
mean_NumTrees               -0.0008308  0.0001553  -5.350 1.12e-07 ***
mean_pavement               -0.6693700  0.1479187  -4.525 6.84e-06 ***
mean_low_vegetation         -1.4197864  0.1249693 -11.361  < 2e-16 ***
mean_high_vegetation        -1.5987011  0.1492561 -10.711  < 2e-16 ***
mean_water                  -6.7044218  0.6942527  -9.657  < 2e-16 ***
---
Signif. codes:  0 ‘***’ 0.001 ‘**’ 0.01 ‘*’ 0.05 ‘.’ 0.1 ‘ ’ 1

Residual standard error: 0.4043 on 897 degrees of freedom
Multiple R-squared:  0.4462,    Adjusted R-squared:  0.4431
F-statistic: 144.5 on 5 and 897 DF,  p-value: < 2.2e-16
```

b) T_{air} perturbation vs land use without Wilhelminenaue

```
lm(formula = mean_Tdiff ~ mean_NumTrees + mean_pavement + mean_low_vegetation +
  mean_high_vegetation, data = df2_slim_subset) # No WHM

Residuals:
   Min     1Q  Median     3Q     Max
-1.26054 -0.23724 -0.02914  0.25693  1.15999

Coefficients:
                    Estimate Std. Error t value Pr(>|t|)
(Intercept)                  0.5231258  0.1151362   4.544 6.60e-06 ***
mean_NumTrees               -0.0011249  0.0001562  -7.203 1.65e-12 ***
mean_pavement               -0.0362742  0.1521322  -0.238    0.812
mean_low_vegetation         -0.1541051  0.1398418  -1.102    0.271
mean_high_vegetation        -1.0387062  0.1445505  -7.186 1.85e-12 ***
---
Signif. codes:  0 ‘***’ 0.001 ‘**’ 0.01 ‘*’ 0.05 ‘.’ 0.1 ‘ ’ 1

Residual standard error: 0.3648 on 646 degrees of freedom
Multiple R-squared:  0.2401,    Adjusted R-squared:  0.2354
F-statistic: 51.03 on 4 and 646 DF,  p-value: < 2.2e-16
```

c) *e* perturbation vs land use including Wilhelminenaue

```
lm(formula = mean_eDiff ~ mean_NumTrees + mean_pavement + mean_low_vegetation +
  mean_high_vegetation + mean_water, data = df2_slim) # With WHM

Residuals:
    Min      1Q  Median      3Q     Max
-0.093084 -0.017061 -0.000955  0.013782  0.188741

Coefficients:
                    Estimate Std. Error t value Pr(>|t|)
(Intercept)                -1.071e-01  8.114e-03 -13.200  < 2e-16 ***
mean_NumTrees               4.980e-05  1.102e-05   4.520 7.02e-06 ***
mean_pavement               6.778e-02  1.050e-02   6.458 1.74e-10 ***
mean_low_vegetation         1.492e-01  8.868e-03  16.826  < 2e-16 ***
mean_high_vegetation        2.015e-01  1.059e-02  19.029  < 2e-16 ***
mean_water                  5.644e-01  4.926e-02  11.458  < 2e-16 ***
---
Signif. codes:  0 '***' 0.001 '**' 0.01 '*' 0.05 '.' 0.1 ' ' 1

Residual standard error: 0.02869 on 897 degrees of freedom
Multiple R-squared:  0.6488,    Adjusted R-squared:  0.6468
F-statistic: 331.4 on 5 and 897 DF,  p-value: < 2.2e-16
```

d) *e* perturbation vs land use without Wilhelminenaue

```
lm(formula = mean_eDiff ~ mean_NumTrees + mean_pavement + mean_low_vegetation +
  mean_high_vegetation, data = df2_slim_subset) # Without WHM

Residuals:
    Min      1Q  Median      3Q     Max
-0.08293 -0.01406 -0.00122  0.01186  0.10081

Coefficients:
                    Estimate Std. Error t value Pr(>|t|)
(Intercept)                -8.144e-02  7.439e-03 -10.949  < 2e-16 ***
mean_NumTrees               8.451e-05  1.009e-05   8.375 3.43e-16 ***
mean_pavement               3.023e-02  9.829e-03   3.076  0.00219 **
mean_low_vegetation         1.041e-01  9.035e-03  11.521  < 2e-16 ***
mean_high_vegetation        1.697e-01  9.339e-03  18.174  < 2e-16 ***
---
Signif. codes:  0 '***' 0.001 '**' 0.01 '*' 0.05 '.' 0.1 ' ' 1

Residual standard error: 0.02357 on 646 degrees of freedom
Multiple R-squared:  0.6229,    Adjusted R-squared:  0.6205
F-statistic: 266.8 on 4 and 646 DF,  p-value: < 2.2e-16
```

Declaration of authorship

I hereby declare that I have authored the Bachelor Thesis titled

“Quantifying the summer urban canopy layer heat island in a mid-sized central European city from noon to midnight:
Effects of land use on spatial patterns and turbulent energy fluxes”

independently based on my work. All direct or indirect sources used are acknowledged as references. This thesis has not been previously published or submitted to any other examination board.

Bayreuth, September 22, 2025

Lars Spakowski